



## Original Paper

# Diamondoids evolution in various phase states of ultra-deep hydrocarbons in Tarim Basin, NW China

Bi-Qing Zhu <sup>a, b</sup>, Quan-You Liu <sup>a, \*</sup>, Hui-Yuan Xu <sup>b</sup>, Dong-Ya Zhu <sup>b</sup>, Peng-Peng Li <sup>a</sup>, Wei-Long Peng <sup>b</sup>, Chi Zhang <sup>c</sup>

<sup>a</sup> Institute of Energy, School of Earth and Space Sciences, Peking University, Beijing, 100871, China

<sup>b</sup> Petroleum Exploration and Production Research Institute, SINOPEC, Beijing, 100083, China

<sup>c</sup> Key Laboratory of Petroleum Resource Research, Institute of Geology and Geophysics, Chinese Academy of Sciences, Beijing, 100191, China



## ARTICLE INFO

## Article history:

Received 17 April 2024

Received in revised form

31 August 2024

Accepted 24 February 2025

Available online 25 February 2025

Edited by Jie Hao

## Keywords:

Diamondoids

Thermal evolution

Molecular markers

Ultra-deep hydrocarbons

Tarim basin

## ABSTRACT

The conventional biomarkers are limited due to the extremely high thermal stresses in ultra-deep hydrocarbon reservoirs. The diamondoid with cage structure has excellent thermal stability and is an effective tool for characterizing the ultra-deep hydrocarbon and linking its source. We investigated the distribution of diamondoids in ultra-deep reservoirs including black oils, volatile oils, and condensates. The source-related diamondoids indicate that crude oils are mainly sourced from marine siliceous shale. The bulk characteristics (e.g. color, density, Sat/Aro) of crude oils reveal the variations of thermal maturity: low maturity for black oils, moderate maturity for volatile oils, and high maturity for condensates. Based on regular variations in the thermal maturity of crude oils, the thermal evolution of diamondoids is characterized. The abundance of C<sub>1</sub>- and C<sub>2</sub>-alkylated diamantanes increases with increasing maturity, and hydrothermal activity may lead to an abnormal increase in the percentage of C<sub>3</sub>-alkylated adamantanes. Despite the higher thermal stability of 4-methyldiamantane (4-MD), a more sensitive change in relative abundance with maturity for 1-methyldiamantane (1-MD) among all methyldiamantanes (MDs) is observed. Ethyl diamondoids are thermally less stable and their derived indices can effectively indicate the thermal maturity of ultra-deep hydrocarbons. The applications of commonly maturity-related indices should be cautious (e.g. MDI), whereas the novel methyl-ethyl diamantane index (MEDI) is highly recommended. The combination of high MAI values and low MEDI values most likely reflects the influence of late-charged light hydrocarbons. Overall, multiple charging and in-reservoir mixing of light hydrocarbons and oils with various maturities constrained the present phase states of ultra-deep oil reservoirs. This study gives a new perspective to understanding the fate of molecular evolution and phase states of hydrocarbons in the ultra-deep basins.

© 2025 The Authors. Publishing services by Elsevier B.V. on behalf of KeAi Communications Co. Ltd. This is an open access article under the CC BY-NC-ND license (<http://creativecommons.org/licenses/by-nc-nd/4.0/>).

## 1. Introduction

Unraveling the origins of ultra-deep hydrocarbons through molecular markers poses a significant challenge, primarily stemming from their susceptibility to degradation under extreme temperatures and pressures. Huang et al. (2016) concurred that biomarker characteristics within the Tarim Basin predominantly arise from extensive secondary alteration processes rather than directly reflecting source facies. Hence, the application of

conventional biomarkers in ultra-deep hydrocarbon petroleum exploration is constrained. For example, there has been an ongoing debate for decades regarding the sources of crude oils in the Tarim Basin. The controversy mainly revolves around whether the Middle-Upper Ordovician source rocks or the Cambrian source rocks constitute the primary source kitchen in Tarim Basin (Hanson et al., 2000; Zhang et al. 2000, 2005; Jia et al., 2010; Cai et al., 2015; Chen et al., 2018; He et al. 2022, 2023b; Bian et al., 2023).

Diamondoids, renowned for their remarkable resistance to thermal stress and biodegradation (Dahl et al., 2003; Azevedo et al., 2008; Li et al., 2014), are frequently found in crude oils and can be notably abundant in condensates which typically lack hopanoid and steroid biomarkers. Diamondoids are extensively utilized in

\* Corresponding author.

E-mail addresses: [liuqy@pku.edu.cn](mailto:liuqy@pku.edu.cn), [qyouliu@sohu.com](mailto:qyouliu@sohu.com) (Q.-Y. Liu).

elucidating the geochemical characteristics of petroleum through quantitative diamondoid analysis (QDA) and quantitative extended diamondoid analysis (QEDA), particularly in light oils and condensates, thereby shedding light on the hydrocarbon origins (Wei et al., 2006c; Moldowan et al., 2015; Gentzis and Carvajal-Ortiz, 2018; Scarlett et al., 2019; Boente et al., 2020; Esegbue et al., 2020; Atwah et al., 2021; Forkner et al., 2021; Walters et al., 2023). Currently, diamondoid-associated indices are extensively employed in investigating the genesis of ultra-deep hydrocarbons within the Tarim Basin. For example, Li et al. (2018) suggested that crude oils from the Tabei and Tazhong areas can be divided into three groups: Group I oils represent late-charged hydrocarbons originating from Middle-Upper Ordovician source rocks with high thermal maturity; Group II oils are early formed hydrocarbons from Cambrian and Lower Ordovician source rocks; Group III oils are sourced from Jurassic or possibly Triassic source rocks. Chai et al. (2020) reported that diamondoid indices reveal significant evaporative fractionation in the oils from the No.1 fault zone, whereas the oil from the No.5 fault zone does not exhibit such fractionation. Similarly, Ma et al. (2021a) suggested that the high concentration of adamantanes in the No.1 fault zone is attributed to late gas charging, while the low concentration of adamantanes in certain reservoirs of the No. 5 fault zone is due to poor preservation conditions. Based on the diamondoid concentration, Zhou et al. (2021) concluded that the Tabei and Tazhong areas experienced at least four episodes of hydrocarbon charging.

Thermal stress intricately correlates with the phase states of ultra-deep hydrocarbons. Elevated thermal stress induces diverse phase states of hydrocarbons (e.g. heavy oil, normal oil, condensates, etc.) directly from kerogen maturation. In addition, the high thermal stress-induced cracking of heavy hydrocarbons can produce light hydrocarbons ( $C_1$ – $C_{12}$ ), leading to variations of phase states in both original and newly formed pools. Hence, it is imperative to understand the maturity variance of ultra-deep hydrocarbons in Paleozoic strata. However,  $\%R_o$  cannot be used in the study of the early Paleozoic thermal history because of a lack of vitrinite macerals (Hanson et al., 2007; Qiu et al., 2012). Measuring the maturity of highly-mature hydrocarbons is also challenging. Given the close association between the distribution of diamondoids and thermal maturity (Chen et al., 1996; Fang et al. 2013, 2015; Jiang et al., 2021; Fu et al., 2023; van der Ploeg et al., 2023; Walters et al., 2023), the thermal transformation of diamondoids offers valuable insights into the maturity variations within highly mature hydrocarbons, and their derived maturity indices are complement to biomarkers. For example, based on the agreement that alkyl-substitutions on bridgehead are more thermally stable than secondary carbon (Clark et al., 1979), several isomerization indices have been proposed to determine the maturity of hydrocarbons (Chen et al., 1996; Zhang et al., 2005). The commonly used indices, including methyl adamantane index (MAI), methyl diamantane Index (MDI), ethyl adamantane index (EAI), dimethyl diamantane index 1 (DMDI-1), dimethyl adamantane index 1 and index 2 (DMAI-1 and DMAI-2), and trimethyl adamantane index 1 and index 2 (TMAI-1 and TMAI-2), have been widely employed for the assessment of maturity in highly-mature hydrocarbons ( $>1.0\%R_o$ ) (Li et al., 2000; Zhang et al., 2005; Fang et al., 2012; Jiang et al., 2018; Mei et al., 2018; Huang et al., 2022; Peng et al., 2022). Nevertheless, maturity-related indices are subject to multifaceted influences. (1) Distinct sedimentary environments and source facies can exert notable effects on maturity indices (e.g. Li et al., 2000; Schulz et al., 2001; Wei et al., 2006a, 2006b, 2006c; de Araujo et al., 2012; Pytlak et al., 2017; Jiang et al., 2018; Jiang et al., 2021), potentially surpassing the influence of thermal stress itself. Walters et al. (2023) also reported that diamondoid maturity indices of lower Eagle Ford oils/condensates are not well-correlated

and appear to be significantly influenced by source facies. (2) The applicability range varies among different maturity indices. According to anhydrous pyrolysis of crude oils, Fang et al. (2012) proposed that MAI, DMAI-1, DMAI-2, TMAI-1, TMAI-2, and EAI are effective for assessment of maturity in a certain range. Fang et al. (2013) subsequently reported that some isomerization ratios of diamondoids (e.g. MAI, DMAI-1, TMAI-1) increase with maturity at  $<2.0\% \text{ Easy}R_o$ , while others (e.g. A/D, MA/MD, DMA/DMD) keep constant. In the hydrothermal pyrolysis of crude oils, Peng et al. (2022) proposed that MDI, EAI, DMAI-1, and DMDI-2 may serve as reliable maturity proxies at  $>1.0\% \text{ Easy}R_o$ , and other isomerization indices (TMAI-1, TMAI-2, and DMAI-2) are effective for the highly mature hydrocarbons at  $>2.0\% \text{ Easy}R_o$ . (3) Various secondary processes, including evaporation fractionation, biodegradation, in-reservoir mixing, and thermochemical sulfate reduction (TSR), can also impact diamondoid indices (Grice et al., 2000; Wei et al., 2007a, 2007b; Gentzis and Carvajal-Ortiz, 2018; Zhu et al. 2019b, 2019c, 2021; Spaak et al., 2020; Jiang et al., 2021; Wang et al., 2021; Chang et al., 2022; Qi et al., 2022; Fu et al., 2023; He et al., 2023b; Walters et al., 2023). Furthermore, Wei et al. (2006b) and Wang et al. (2023c) both demonstrated that diamondoids could be destructed under high temperatures, leading to the formation of polycyclic aromatic hydrocarbons. Xu et al. (2022) reported that oils in the Shuntuoguo (STGL) area might be altered by hydrothermal activity. As a result, a reversal in the distribution and concentration of diamondoids may likely occur in the context of high thermal stress, as evidenced by some pyrolysis experiments (Fang et al., 2012; Peng et al., 2022).

The current challenge lies in the significant disparities between simulated laboratory experiments and actual geological processes, prompting the inquiry into the thermal transformation of various diamondoid compounds in practical reservoirs. Despite the large amounts of diamondoid maturity indices, the challenge persists in selecting the most suitable ones. This emphasizes the imperative of identifying maturity-dependent diamondoids tailored to the geological context of individual basins. To give insights into these problems, we systematically collected more than 20 oil samples of various phase states from ultra-deep reservoirs in the STGL area, Tarim basin. Based on the comprehensive analysis of diamondoids in petroleum, the purposes of this study are to (1) investigate the geochemical characteristics of hydrocarbons in ultra-deep reservoirs, (2) identify the impacts of thermal stress on the distribution of diamondoids and (3) reveal the origin for the multiple phase states (e.g. black oils, volatile oils, condensates) of ultra-deep hydrocarbons.

## 2. Geological setting

The Tarim Basin, which developed on an Archean and Proterozoic metamorphosed basement (Qiu et al., 2012), is a complex superimposed basin with an area of about  $56 \times 10^4 \text{ km}^2$ . The basin is overlain by a well-developed Neoproterozoic-Quaternary sedimentary sequence, with a maximum thickness of 16,000 m. The Cambrian–Lower Ordovician strata comprise shallow marine to lagoonal carbonates with a depth of 3 km, while the Middle-Upper Ordovician strata were deposited during a marine transgression event (Zhang et al., 2005). The marine strata, marine–continental transitional strata, and terrestrial strata were developed during the Sinian-Devonian, Carboniferous-Permian, and Triassic-Quaternary, respectively. The Basin has experienced six major regional tectonic orogenesis: late Caledonian, early Hercynian, end Hercynian, Indosinian, end Yanshan, and late Himalayan (Pang et al., 2018). Among these, The three main oil and gas charging periods consist of middle-late Caledonian (463.2–414.9 Ma), late Hercynian (312.9–268.8 Ma), and Himalayan (22.0–4.8 Ma) (Yang

et al., 2021). The late Hercynian, which almost coincides with the timing of the early Permian Tarim Large Igneous Province (TLIP) (Yang et al., 2013), is considered to be the key period for oil and gas charging (Chang et al., 2013; Zhang et al., 2018).

The STGL area is located in the desert-covered area of the central Tarim Basin, which is adjacent to the Manjar Depression and Awati Depression, respectively (Fig. 1(a) and (b)). The Ordovician-Cambrian strata in the STGL area of the Tarim Basin in NW China are typical sites for ultra-deep petroleum exploration, with an average depth of exceeding 7300 m, of which Shunbei (SB) oil and gas field and Fuman (FM) Oilfield are the most productive. By the end of 2021, the Shunbei oil and gas field has submitted a cumulative total of more than  $2 \times 10^8$  t of proven oil and gas reserves, with approximately  $17 \times 10^8$  t of oil and gas equivalents distributed along 18 main faults (Ma et al., 2022). As of June 2022, nine wells producing 1000 t of crude oil per day had been discovered in the Fuman Oilfield, with oil and gas reserves of approximately  $10 \times 10^8$  t (Han et al., 2023). The exploration prospect of the STGL area is vast, and the deep oil and gas resources are expected to become the replacement field for increasing oil and gas reserves in the future. The Fuman oil field covers an area of approximately 7000 km<sup>2</sup> and can be subdivided into Yueman (YM), Fuyuan (FY),

Hade (HD), Yuke (YK), Manshen (MS), and Guole (GL) areas (Wang et al., 2023b). The SB oil and gas field is mainly named according to the number of major faults. For example, the wells in SB1 and SB4 correspond to the No.1 and No.4 Faults, respectively. The STGL was formed in the middle Caledonian, and the Lower Palaeozoic strata comprise a complete source-reservoir-cap assemblage. Multi-stage faults were developed during the Caledonian-Hercynian period, which favored fracture development and fluid modification to form multiple types of reservoirs, and the giant mudstones deposited during the Late Ordovician can be a regional cap layer. From top to bottom, the Ordovician strata consists of Sangtamu Formation (O<sub>3s</sub>), Lianglitage Formation (O<sub>3l</sub>), and Tumuxiuke Formation (O<sub>3t</sub>) in the Upper Ordovician, Yijianfang Formation (O<sub>2y</sub>) in the Middle Ordovician, Yingshan Formation (O<sub>1-2y</sub>) in the Lower–Middle Ordovician, Penglaiba Formation (O<sub>1p</sub>) in the Lower Ordovician, respectively (Fig. 1(c)) (Zhu et al., 2019c). Among them, the Yijianfang Formation (O<sub>2y</sub>) and Yingshan Formation (O<sub>1-2y</sub>) are the main targets for petroleum exploration (Chen et al., 2021). A set of source rocks in Yuertusi formation (Є<sub>1y</sub>) was developed under the early tension background of the Early Cambrian, with the sedimentary facies of continental shelf to slope. Siliceous black shales with high TOC (2%–6%) are developed within the Yuertusi

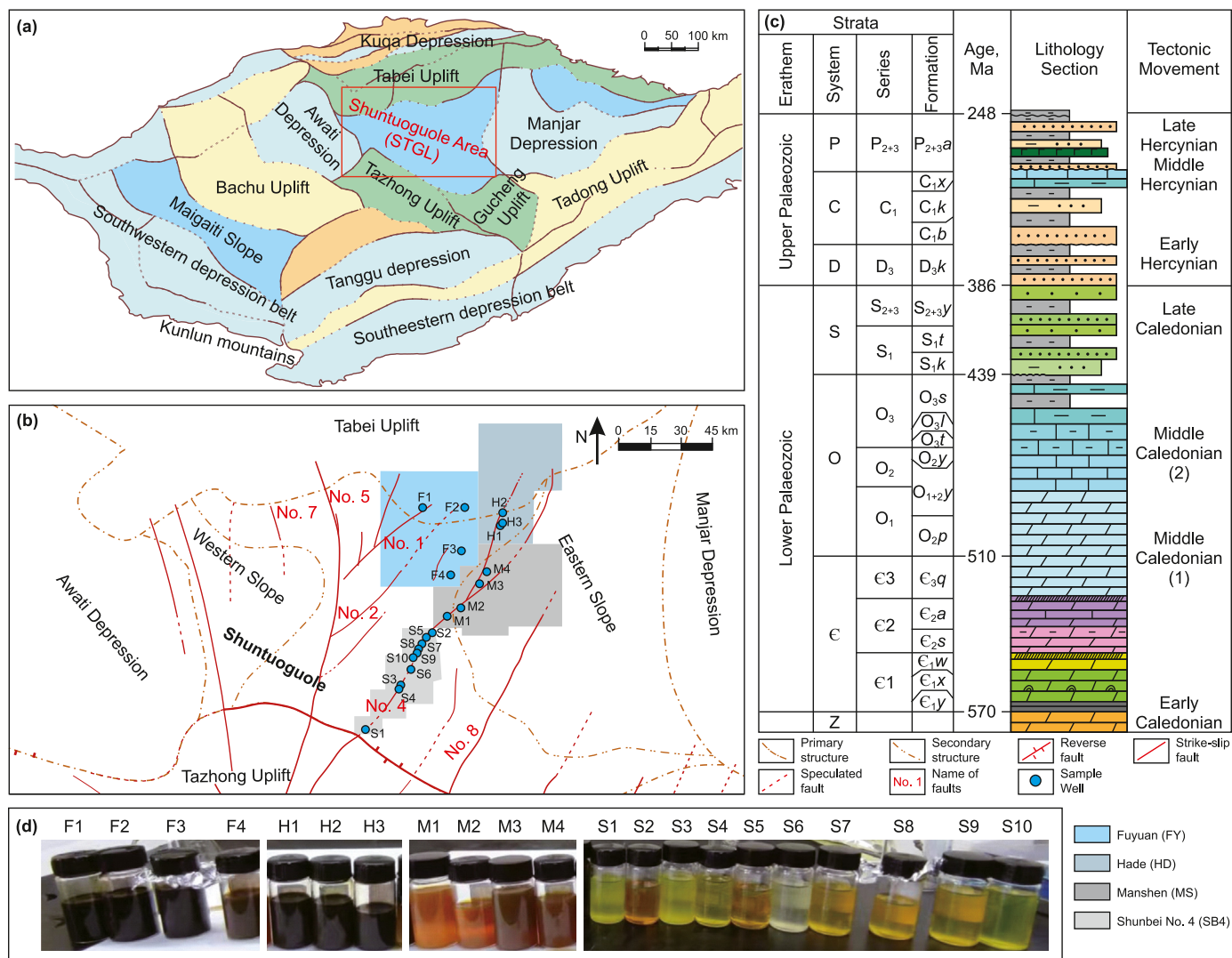


Fig. 1. (a) Map showing major tectonic domains and location of the Shuntuoguole area in the Tarim Basin, Western China; (b) Location of sample wells, modified from Ma and Qi (2023); (c) Palaeozoic stratigraphic column of Tarim basin (modified from Zhu et al. (2019c)); (d) Regular variations of colors in all samples.

Formation (O<sub>2</sub>Y), which is widely distributed in the STGL area with an area of approximately 260,000 km<sup>2</sup> and is considered to be the most important source of hydrocarbons (Chen et al., 2018; Wang et al., 2021). Due to the low geothermal gradient, the Yuertusi source rock is still in the wet gas stage during the Himalayan period, as well as the potential to form giant oil and gas fields in the late stage (Qi, 2016).

Reservoir pressures are between 70 and 85 MPa at depths greater than 6500–7500 m, with pressure coefficients between 1.2 and 1.7 and temperatures ranging between 140 and 172 °C (Zhu et al., 2019a). In the SB area, temperatures in Ordovician reservoirs do not exceed 180 °C even beyond 8000 m (Ma et al., 2021b). Tian et al. (2006) reported that the crude oil in a separate phase is stable before 1.70%–1.75% EasyR<sub>o</sub>. This suggested that the oil has barely cracked despite high temperatures (i.e., >170 °C). At geological heating rates in Tarim basins, the initial temperature for oil cracking is about 148–162 °C and reached the endpoint at 245–276 °C (Wang et al., 2006). Specifically, the preservation threshold of a discrete oil phase extends from approximately 178 °C under slow geological heating conditions to 206 °C with rapid geological heating rates (Ma, 2016). Zhu et al. (2020) concluded that the threshold temperature for intense oil cracking until its extinction is calculated as 210 °C. The mixtures of heavy hydrocarbons and hydrogen become more stable than pure methane between 1000 and 2000 K and  $P \geq 4$  GPa, as evidenced by simulations experiments conducted by (Spanu et al., 2011). The preservation of heavy hydrocarbons is indeed promising in ultra-deep reservoirs in the Tarim basin due to the low current geothermal gradient and initial continuously slow burial followed by rapid late burial.

### 3. Samples and methods

#### 3.1. Samples

This study collected 21 oil samples from typical production wells with depths exceeding 7000 m in STGL area, Tarim basin. Four samples of black oils from the FY area, three samples of black oils from the HD area, four samples of volatile oils/condensates from the MS area, and ten samples of condensates from the SB4 area (Fig. 1(d), Table 1). The phase states of crude oils have also been

evidenced by previous studies (Bian et al., 2023; Ma and Qi, 2023; Wang et al., 2023b; Peng et al., 2024). The detailed information of all samples is shown in Table 1. To reflect regional variations, the discussion will follow the order of the FY to HD to MS to SB4 (hereafter referred to as the FHMSB profiles), corresponding with the changing trends of oil colors (Fig. 1(d)).

#### 3.2. SARA fractionation

SARA (Saturate, Aromatics, Resins, Asphaltenes) fractionation was performed to characterize the bulk geochemistry of crude oils. The crude oils (about 30 mg) were deasphalted with excess *n*-hexane. Subsequently, the separation was performed on a liquid chromatographic column (3 g of silica gel and 1 g of alumina). The de-asphaltene fractions were separated into saturated hydrocarbons, aromatic hydrocarbons, and resins by using successive *n*-hexane, dichloromethane (DCM)/*n*-hexane (2:1, v:v), and dichloromethane/methanol (1:1, v:v) as eluting solvents, respectively (Xu et al., 2022). Finally, the asphaltenes were dissolved in DCM for weighing. Under the same conditions, the bottle containing saturated hydrocarbon, aromatic hydrocarbon, resin, and asphaltene components was weighed at 30-min intervals after the solvent had evaporated and dried up. The constant weight was documented when the difference between the two measurements was not greater than 0.3 mg. However, due to the extreme volatility and loss of light oil/condensate, the sum of SARA fraction is less than 100% (Table 1). Finally, the eluted saturated hydrocarbons were prepared for GC-MS analysis.

#### 3.3. Gas chromatography-mass spectrometry (GC-MS)

The analysis of gas chromatography-mass spectrometry (GC-MS) was performed using Agilent 6890 GC with an Agilent 5975B MS. The gas chromatograph was equipped with a J&W HP-5ms fused silica capillary column (60 m × 0.25 mm × 0.25 μm). The inlet temperature was 300 °C. Helium (99.995%) was used as the carrier gas, with a constant flow rate of 1.0 mL/min. The oven temperature was initially held at 50 °C for 1 min, then was programmed to 100 °C at 20 °C/min, finally was programmed to 310 °C at 3 °C/min, and was held for 10 min. The ion source of the mass

**Table 1**  
Bulk geochemical characteristics for oils in STGL area.

Location	Code	Well	Formation	Depth, m	Density, g/cm <sup>3</sup>	Wax, %	Viscosity, mPa·s	GOR, m <sup>3</sup> /m <sup>3</sup>	Fraction groups, %				Sat/Aro
									Sat	Aro	Resin	Asphalt	
FY	F1	FY103-H3	O	7295–7582	0.81	10.90	2.71	160.84	60.36	8.77	2.72	2.27	6.88
	F2	FY201-H6	O	7126–7363	0.84	14.70	3.12	110.76	53.17	11.75	1.39	0.93	4.53
	F3	FY210H	O	7446–7693.9	0.81	11.20	1.79	194.16	59.46	8.19	1.41	1.98	7.26
	F4	FY216H	O <sub>2</sub> Y	7492–7862	0.80	11.10	1.57	268.21	56.25	5.55	1.63	0.96	10.13
HD	H1	HD32-H9	O <sub>2</sub> Y	7256–7634	0.82	10.80	2.08	156.08	59.82	8.15	1.41	0.92	7.34
	H2	HD302H	O <sub>2</sub> Y	7066–7225.66	0.82	11.40	2.25	162.13	65.87	9.71	1.64	0.22	6.79
	H3	HD32-H1	O <sub>2</sub> Y	7219.36–7703	/	/	/	197.03	66.37	9.44	2.41	0.60	7.03
MS	M1	ManS4	O <sub>2</sub> Y	7573–8208	0.79	10.50	1.26	604.84	61.50	3.48	0.80	0.00	17.69
	M2	ManS3-H5	O <sub>2</sub> Y	7485–8410	0.79	14.80	1.25	607.02	64.74	3.69	0.76	0.00	17.56
	M3	ManS502H	O <sub>2</sub> Y	7370.5–7820.00	0.79	10.40	1.22	398.69	65.57	3.52	0.44	0.00	18.65
	M4	ManS5-H9	O <sub>2</sub> Y	7459–7935	0.80	10.60	1.56	358.05	60.89	3.77	0.85	0.00	16.15
SB4	S1	SHB4-1H	O <sub>2</sub> Y + O <sub>1-2</sub> Y	7394–7925.59	0.76	4.00	/	1866.00	59.55	2.89	1.13	0.00	20.61
	S2	SHB44X	O <sub>2</sub> Y + O <sub>1-2</sub> Y	7493.49–7882.55	0.79	3.60	2.04	795.00	64.54	4.10	0.67	0.00	15.72
	S3	SHB4-8H	O <sub>2</sub> Y + O <sub>1-2</sub> Y	7532–8378	0.74	1.60	/	2256.00	58.96	1.98	0.99	0.00	29.75
	S4	SHB46X	O <sub>1-2</sub> Y	8590–8670	0.78	/	/	2074.00	55.27	1.61	2.49	0.00	34.35
	S5	SHB4-5H	O <sub>1-2</sub> Y	7729–8850.34	0.79	/	/	1060.00	66.86	2.71	0.41	0.00	24.70
	S6	SHB41X	O <sub>2</sub> Y + O <sub>1-2</sub> Y	7531.00–7984.10	0.76	1.74	1.90	2888.00	49.01	1.66	0.40	0.00	29.52
	S7	SHB43X	O <sub>2</sub> Y + O <sub>1-2</sub> Y	7566–7995	0.79	2.70	/	1040.00	62.67	2.13	0.82	0.00	29.38
	S8	SHB4-9H	O <sub>2</sub> Y + O <sub>1-2</sub> Y	7597–8110.17	0.79	3.50	/	1263.00	65.09	2.42	0.81	0.00	26.93
	S9	SHB4-6H	O <sub>1-2</sub> Y	7571.75–8356.02	0.78	/	/	1350.00	56.44	2.61	1.66	0.00	21.64
	S10	SHB45X	O <sub>2</sub> Y + O <sub>1-2</sub> Y	7668–8845	0.79	2.10	/	1443.00	55.41	2.11	1.85	0.00	26.25

spectrometer was operated in EI mode at 70 eV with a temperature of 230 °C; Saturated hydrocarbons of all samples (1.5  $\mu\text{L}$ ) were injected at a splitless mode (20:1). The full scan (50–570 amu) and selected ion monitoring (SIM) mode were used to acquire MS data. The identification of diamondoid hydrocarbons was based on retention times, and references (Wei et al., 2007c; Liang et al., 2012; Walters et al., 2023). The relative abundance of the diamondoid hydrocarbons was determined from peak area (using selected mass chromatograms for the integration of the compounds) by Agilent Masshunter Qualitative Analysis 10.0 software. The identification results are shown in Fig. 2. The formulas and abbreviations of individual diamondoid compounds are shown in Table 2. It is noteworthy that the peak before 2-MA is identified as 1,2,3,4-alkylbenzene (1,2,3,4-TeMB) by comparing the mass chromatograms and spectrums with previous studies (Jia et al., 2007; Zhang et al., 2014; Cheng et al., 2015; Zhan et al., 2023; Meng et al., 2024).

## 4. Results

### 4.1. Bulk geochemistry

Along the FHMSB profile, the bulk characteristics of total oils samples show a regular variation with depth which corresponds to the increasing thermal stress (Table 1). In particular, the crude oils exhibit significant variations in colors (Fig. 1(d)). In the FY and HD areas, crude oils are predominantly characterized as black oils, with a density ranging from 0.80 to 0.84  $\text{g}/\text{cm}^3$ , wax content ranging from 10.80% to 14.70%, viscosity ranging from 1.57 to 3.12  $\text{mPa s}^{-1}$ , gas-oil ratio (GOR) ranging from 110.76 to 268.21  $\text{m}^3/\text{m}^3$ , and Saturate hydrocarbons/Aromatic hydrocarbons (Sat/Aro) ranging

from 2.40 to 10.13. It is noteworthy that well F4 exhibits a tiny difference due to the high Sat/Aro ratio and GOR. In the MS area, the yellow-brown crude oils are predominantly characterized as volatile oils/condensates, with a density ranging from 0.79 to 0.80  $\text{g}/\text{cm}^3$ , wax content ranging from 10.40% to 14.80%, viscosity ranging from 1.22 to 1.56  $\text{mPa s}^{-1}$ , GOR ranging from 358.05 to 607.02  $\text{m}^3/\text{m}^3$ , and Sat/Aro ranging from 16.15 to 18.15. In the SB4 area, the light-yellow crude oils are characterized as condensates, with a density ranging from 0.76 to 0.79  $\text{g}/\text{cm}^3$ , wax content ranging from 1.6% to 4.0%, viscosity ranging from 1.90 to 2.04  $\text{mPa s}^{-1}$ , GOR ranging from 795 to 2888  $\text{m}^3/\text{m}^3$ , and Sat/Aro ranging from 15.72 to 34.35.

### 4.2. Diamondoids

The mass chromatograms of adamantanes and diamantanes of typical wells are illustrated in Figs. 3 and 4, respectively. All maturity-related indices calculated in this study are summarized in Table 3. Ternary distributions of representative compounds are provided in Supplementary Table S1, while the formulas for all diamondoid indices are detailed in the Appendix and listed in Supplementary Table S2.

Notable variations are observed in the methyladamantanes (MAs) and dimethyladamantane (DMAs) among all adamantanes (Fig. 3). The concentration of 1-MA shows a gradual increase along the FHMSB profile, albeit with modest increments. The MAI values range from 0.59 to 0.65 in FY area, 0.64 to 0.66 in HD area, 0.65 to 0.70 in MS area, and 0.67 to 0.71 in SB4 area. While the variation range of MAI is not extensive, a discernible pattern of MAI value fluctuation is still observable. Additionally, the abundance of

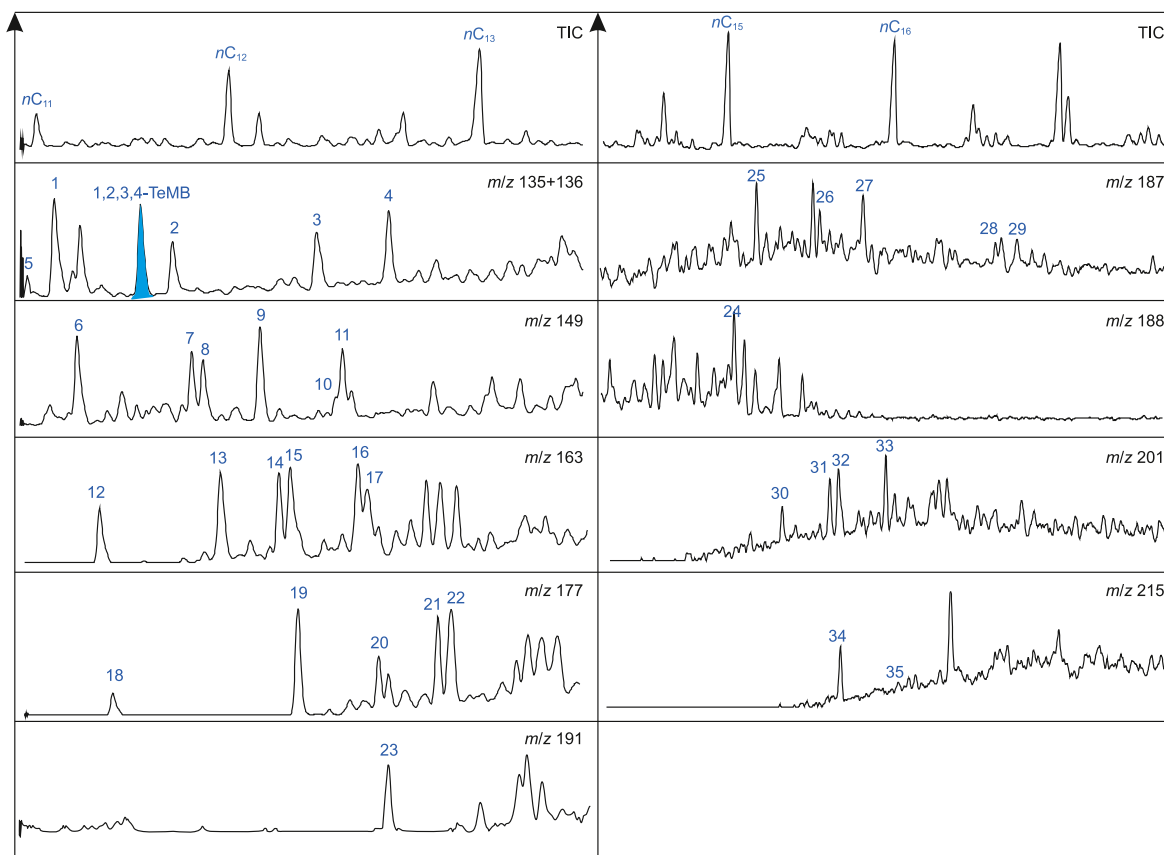


Fig. 2. Identification results of diamondoid compounds of well F1. 1,2,3,4-TeMB: 1,2,3,4-Tetramethylbenzene.

**Table 2**  
Identification and abbreviations of diamondoid compounds.

No.	Name	Abbreviation	Formula	M+ (m/z)	Peak
1	1-Methyladamantane	1-MA	C <sub>11</sub> H <sub>18</sub>	150	135
2	2-Methyladamantane	2-MA	C <sub>11</sub> H <sub>18</sub>	150	135
3	1-Ethyladamantane	1-EA	C <sub>12</sub> H <sub>20</sub>	164	135
4	2-Ethyladamantane	2-EA	C <sub>12</sub> H <sub>20</sub>	164	135
5	Adamantane	A	C <sub>10</sub> H <sub>16</sub>	136	136
6	1,3-Dimethyladamantane	1,3-DMA	C <sub>12</sub> H <sub>20</sub>	164	149
7	cis1,4-Dimethyladamantane	1,4-DMA (cis)	C <sub>12</sub> H <sub>20</sub>	164	149
8	trans1,4-Dimethyladamantane	1,4-DMA (trans)	C <sub>12</sub> H <sub>20</sub>	164	149
9	1,2-Dimethyladamantane	1,2-DMA	C <sub>12</sub> H <sub>20</sub>	164	149
10	2,4 + 2,6-dimethyladamantane	2,4 + 2,6-DMA	C <sub>12</sub> H <sub>20</sub>	164	149
11	1-Ethyl-3-methyladamantane	1-E-3-MD	C <sub>13</sub> H <sub>22</sub>	178	149
12	1,3,5-Trimethyladamantane	1,3,5-TMA	C <sub>13</sub> H <sub>26</sub>	182	163
13	1,3,6-Trimethyladamantane	1,3-TMA	C <sub>13</sub> H <sub>26</sub>	182	163
14	cis1,3,4-Trimethyladamantane	1,3,4-TMA	C <sub>13</sub> H <sub>26</sub>	182	163
15	trans1,3,4-Trimethyladamantane	1,3,4-TMA	C <sub>13</sub> H <sub>26</sub>	182	163
16	1,2,3-Trimethyladamantane	1,2,3-TMA	C <sub>13</sub> H <sub>26</sub>	182	163
17	1-Ethyl-3,5-dimethyladamantane	1-E-3,5-TeMA	C <sub>14</sub> H <sub>24</sub>	192	163
18	1,3,5,7-Tetramethyladamantane	1,3,5,7-TeMA	C <sub>14</sub> H <sub>24</sub>	192	177
19	1,2,5,7-Tetramethyladamantane	1,2,5,7-TeMA	C <sub>14</sub> H <sub>24</sub>	192	177
20	1,3,5,6-Tetramethyladamantane	1,3,5,6-TeMA	C <sub>14</sub> H <sub>24</sub>	192	177
21	1,2,3,5-Tetramethyladamantane	1,2,3,6-TeMA	C <sub>14</sub> H <sub>24</sub>	192	177
22	1-Ethyl-3,5,7-Trimethyladamantane	1-E-3,5,7-TMA	C <sub>15</sub> H <sub>26</sub>	206	177
23	1,2,3,5,7-Pentamethyladamantane	1,2,3,5,7-PMA	C <sub>15</sub> H <sub>26</sub>	206	191
24	Diamantane	D	C <sub>14</sub> H <sub>20</sub>	188	188
25	4-Methyldiamantane	4-MD	C <sub>15</sub> H <sub>22</sub>	202	187
26	1-Methyldiamantane	1-MD	C <sub>15</sub> H <sub>22</sub>	202	187
27	3-Methyldiamantane	3-MD	C <sub>15</sub> H <sub>22</sub>	202	187
28	1-Ethyldiamantane	1-ED	C <sub>16</sub> H <sub>24</sub>	216	187
29	3-Ethyldiamantane	3-ED	C <sub>16</sub> H <sub>24</sub>	216	187
30	4,9-Dimethyldiamantane	4,9-DMD	C <sub>16</sub> H <sub>24</sub>	216	201
31	1,4+2,4-Dimethyldiamantane	1,4+2,4-DMD	C <sub>16</sub> H <sub>24</sub>	216	201
32	4,8-Dimethyldiamantane	4,8-DMD	C <sub>16</sub> H <sub>24</sub>	216	201
33	3,4-Dimethyldiamantane	3,4-DA	C <sub>16</sub> H <sub>24</sub>	216	201
34	1,4,9-Trimethyldiamantane	1,4,9-TMD	C <sub>17</sub> H <sub>26</sub>	230	215
35	3,4,9-Trimethyldiamantane	3,4,9-TMD	C <sub>17</sub> H <sub>26</sub>	230	215

compound Z gradually decreases along the FHMSB profile. The abundance of 1,3-DMA shows a gradual increase, while the relative abundance of 1,2-DMA decreases gradually. The DMAI-1 values in FY, HD, MS, and SB4 areas are 0.40–0.48, 0.49–0.50, 0.54–0.58, and 0.55–0.60, respectively. Conversely, the variation in DMAI-2 values was not significant. Relative percentages of 1,3-DMA in FY, HD, MS, and SB4 areas are 25%–28%, 29%–30%, 30%–36%, and 31%–35%, respectively (Table S1). The trimethyladamantanes (TMAs) and pentamethyladamantane (PMA) show minimal variations. The TMAI-1 and TMAI-2 values of all samples are 0.22–0.28 and 0.35–0.42 respectively. The relative percentages of 1,3,5-TMA, 1,3,6-TMA, and 1,3,4-TMA remain consistently within a narrow range across all samples. However, interesting variations were observed in the tetramethyladamantanes (TeMAs) (Fig. 4). Along the FHMSB profile, the newly introduced tetramethyl-ethyl adamantane index (TeMEAI = 1,2,5,7-TeMA/1-E-3,5,7-TMA) evidences a gradual yet modest rise, with values in FY, HD, MS, and SB4 areas ranging from 0.95 to 1.20, 1.16 to 1.20, 1.27 to 1.40, and 1.30 to 1.47, respectively.

Significant changes are observed primarily in the methyldiamantanes (MDs) among all diamantanes (Fig. 4). The relative abundance of 4-MD appears to increase gradually along the FHMSB profile. However, the MDI values of all samples range between 0.40 and 0.50, showing no significant variations (Table 3). In contrast, the relative percentages of 4-MD, 1-MD, and 3-MD exhibit systematic changes along the FHMSB profile. Particularly noteworthy is the gradual increase in the relative percentage of 1-MD. This observation suggests that the transformation relationships among 4-MD, 1-MD, and 3-MD may not align precisely with previous assumptions. The abundance changes of MDs relative to

ethyldiamantanes (EDs) exhibit a progressive linear trend, resulting in the proposal of methyl-ethyl diamantane index (MEDI = 4-MD/[4-MD+1-ED+2-ED]). The MEDI values in oils from FY, HD, MS, and SB4 areas are 0.50–0.66, 0.53–0.59, 0.71–0.81, and 0.79–0.90, respectively. Variations in the abundance of dimethyldiamantanes (DMDs) across all samples are nuanced, with DMDI-1 and DMDI-2 indices ranging from 0.32 to 0.41 and 0.30 to 0.40, respectively. The relative percentage of 4,9-MD, 4,8-MD and 3,4-MD are 19%–24%, 33%–45% and 36%–45%, respectively (Table S1).

## 5. Discussions

### 5.1. Marine-sourced diamondoids

Gordadze (2008) observed that crude oils sourced from clay-poor and algal organic matter (OM) sources tend to exhibit higher MAI values and lower concentrations of A+1-MA+2-MA, whereas crude oil derived from clay-rich and higher plant sources tends to show relatively lower MAI values and higher concentrations of A+1-MA+2-MA. Hence, the MAI values of all the samples in STGL area range from 0.6 to 0.8, indicative of marine sources. Additionally, the relative percentage of  $\sum C_{11s}$ ,  $\sum C_{12s}$ , and  $\sum C_{13s}$  (Table S1) can serve as indicators of source facies. Compared to marine sources, terrestrial source rocks exhibit a higher relative percentage of  $\sum C_{13s}$  (Gordadze, 2008). It can be observed that all samples in this study fall between marine and terrigenous sources (Fig. 5(a)), overlapping with the distribution range of marine silycalites. The well F1, which is located at the termination of the No.1 Fault in STGL area, exhibits an exceptionally high proportion of  $\sum C_{13s}$ . We speculate that this could be attributed to the

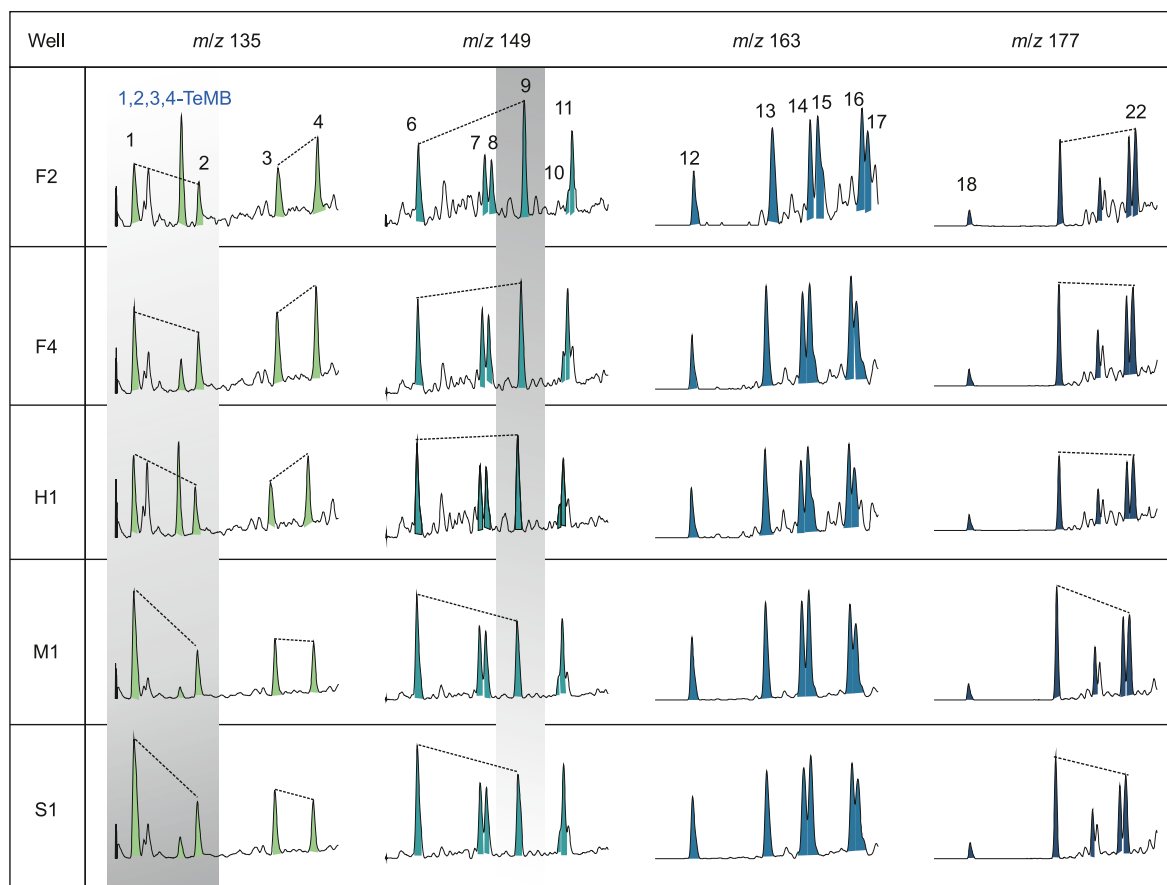


Fig. 3. The mass chromatograms of adamantanes from typical wells in STGL area.

hydrothermal alteration (Xu et al., 2022). Due to the enhanced thermal stability, the distribution of dimethyldiamantanes (DMDs) could serve as source-dependent indices. Previous studies have shown that the distribution of 4,9-DMD, 4,8-DMD, and 3,4-DMD can distinguish source facies including marine carbonate, marine shale, and coal (Schulz et al., 2001; Walters et al., 2023). Correspondingly, the ternary plot of 4,9-DMD, 4,8-DMD, and 3,4-DMD indicates that all samples originate mainly from marine shale (Fig. 5(b)). In summary, the crude oils in STGL area are most likely derived from the marine siliceous shales of the Cambrian Yuertusi Formation.

## 5.2. Thermal maturity

### 5.2.1. Maturity based on bulk geochemistry

Under conditions of high thermal stress, biomarker degradation can be severe, complicating the assessment of maturity in ultra-deep hydrocarbons. The classical theory of kerogen maturation suggests that the general properties of oil, such as density and the ratio of Sat/Aro, are indicative of thermal maturity (Tissot et al., 1984; Killops and Killops, 2004). Typically, oils and condensates of higher maturity exhibit lower densities and elevated Sat/Aro values. For instance, Hackley et al. (2021) demonstrated a robust correlation between Sat/Aro and %R<sub>MPI</sub> ( $R^2 = 0.88$ ) in oils from the Upper Devonian Berea Sandstone in northeastern Kentucky. Fu et al. (2023) identified that black and volatile oils predominantly originate during the peak oil window, whereas gas condensates are products of the late oil stage. Claypool and Mancini (1989) noted that GOR is well correlated with the extent of oil cracking (EOC)

which results mostly from thermal maturity, although usually affected by fractionation and diffusion processes within reservoirs, and gas washing during migration (Dahl et al., 1999).

This study unveils a coherent pattern in the bulk geochemical characteristics (e.g. color, density, Sat/Aro, GOR) of crude oils corresponding to maturity progression (Fig. 6). Along the FHMSB profile, there is a gradual escalation in reservoir burial depths alongside increasing thermal stress. Oils from the FY and HD areas are characterized by high density and high wax content, accompanied by low GOR and low Sat/Aro values. In contrast, well F4 displays low density, high GOR, and elevated Sat/Aro values, indicative of advanced maturity, consistent with its proximity to the MS area. Oils in MS area exhibit low density, high wax content, and moderate GOR and Sat/Aro values. In contrast, oils in the SB4 area exhibit low density and wax content, along with high GOR and Sat/Aro values. These consistent bulk characteristics suggest low maturity for oils in FY and HD areas, moderate maturity for oils in the MS area, and high maturity for oils in the SB4 area. Notably, the high wax content in FY, HD, and MS areas suggests light hydrocarbon charging, with oil reservoirs experiencing mixed charging by early oil with low maturity and late light hydrocarbons with high maturity, leading to wax precipitation. Conversely, the low wax content in the SB4 area indicates the high maturity of crude oils.

### 5.2.2. Alkylated diamondoids

The distribution of C<sub>0</sub>-C<sub>5</sub> alkylated diamondoids provides a robust proxy for hydrocarbon maturity. Pyrolysis studies reveal that the relative abundance of C<sub>1</sub>-, C<sub>2</sub>-, C<sub>3</sub>-, and C<sub>4</sub>-alkylated adamantanes increases with increasing maturity, whereas the

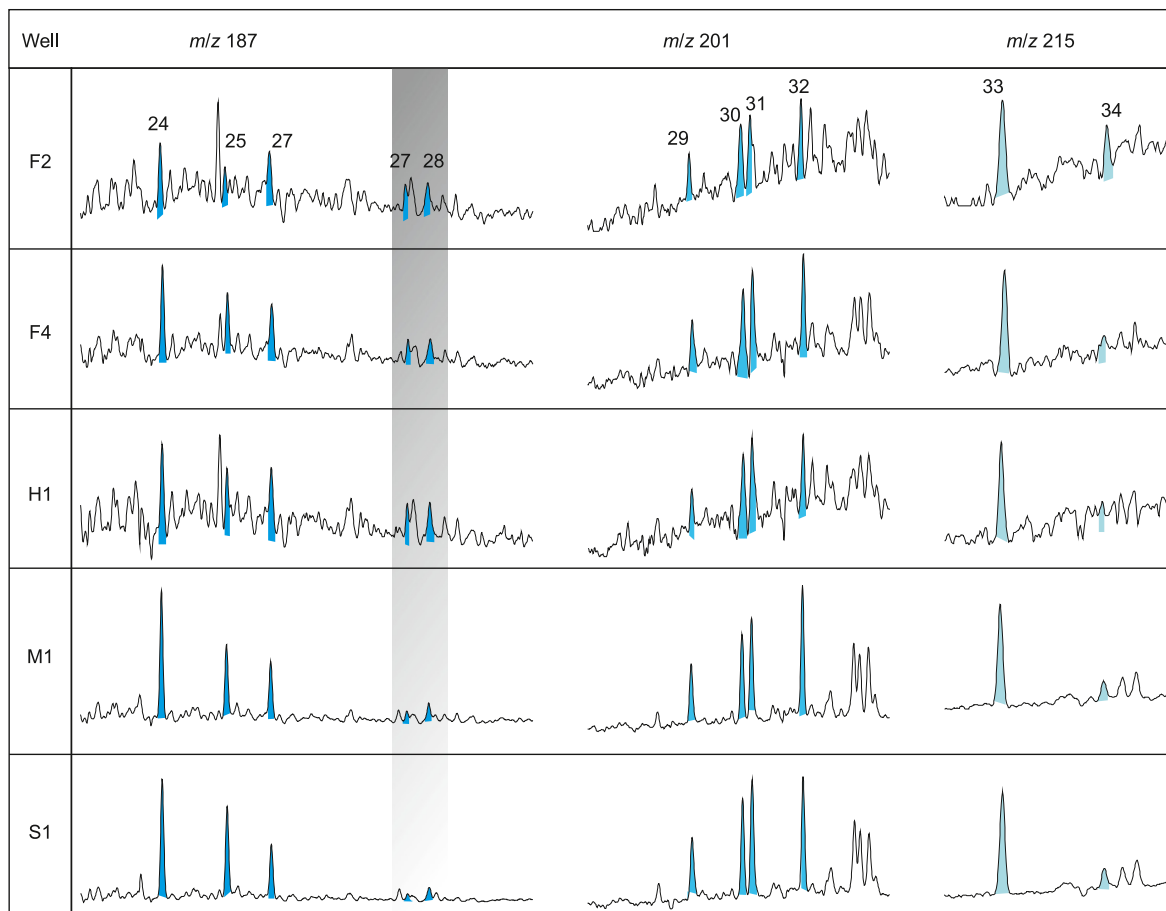


Fig. 4. The mass chromatograms of diamantanes from typical wells in STGL area.

Table 3  
Maturity-related indices of diamondoids.

Type	Indices	Well No.																				
		F1	F2	F3	F4	H1	H2	H3	M1	M2	M3	M4	S1	S2	S3	S4	S5	S6	S7	S8	S9	S10
Adamantanes-associated	MAI	0.65	0.59	0.59	0.60	0.64	0.66	0.65	0.70	0.66	0.65	0.66	0.68	0.70	0.68	0.68	0.71	0.67	0.69	0.69	0.69	0.67
	EAI	0.43	0.39	0.41	0.43	0.40	0.39	0.40	0.53	0.49	0.46	0.46	0.55	0.53	0.55	0.56	0.54	0.61	0.54	0.54	0.56	0.51
	DMAI-1	0.48	0.40	0.43	0.47	0.50	0.50	0.49	0.58	0.57	0.55	0.54	0.59	0.60	0.59	0.57	0.60	0.55	0.59	0.58	0.56	0.55
	DMAI-2	0.40	0.40	0.38	0.38	0.42	0.43	0.43	0.49	0.43	0.42	0.41	0.45	0.46	0.44	0.42	0.44	0.41	0.44	0.43	0.42	0.41
	TMAI-1	0.22	0.22	0.22	0.22	0.24	0.28	0.27	0.24	0.25	0.25	0.25	0.25	0.26	0.25	0.25	0.25	0.22	0.24	0.24	0.23	0.22
	TMAI-2	0.37	0.36	0.35	0.35	0.37	0.40	0.39	0.39	0.39	0.41	0.40	0.42	0.41	0.42	0.41	0.41	0.38	0.41	0.40	0.39	0.37
	TeMEAI	1.20	0.95	1.12	1.16	1.16	1.20	1.20	1.40	1.27	1.27	1.28	1.30	1.41	1.38	1.41	1.39	1.47	1.33	1.36	1.35	1.46
	B/(B+S)A	0.24	0.30	0.30	0.31	0.34	0.36	0.35	0.38	0.36	0.35	0.35	0.38	0.39	0.37	0.36	0.38	0.34	0.37	0.37	0.35	0.34
	MAs/DMAAs	0.46	0.41	0.40	0.37	0.45	0.47	0.48	0.47	0.45	0.41	0.46	0.46	0.45	0.42	0.40	0.43	0.34	0.42	0.43	0.41	0.38
	MAs/TMAAs	0.10	0.42	0.40	0.37	0.48	0.61	0.56	0.45	0.48	0.43	0.49	0.47	0.46	0.42	0.41	0.44	0.32	0.41	0.42	0.39	0.35
DMAAs/TMAAs	0.22	1.02	1.00	1.01	1.08	1.31	1.17	0.95	1.06	1.05	1.08	1.04	1.02	1.00	1.02	1.03	0.94	0.99	0.99	0.96	0.93	
Diamantanes-associated	MDI	0.40	0.46	0.46	0.45	0.47	0.43	0.48	0.50	0.44	0.46	0.45	0.45	0.44	0.47	0.47	0.45	0.48	0.46	0.46	0.45	0.46
	MEDI	0.50	0.66	0.58	0.66	0.59	0.53	0.58	0.81	0.71	0.74	0.73	0.83	0.79	0.86	0.86	0.81	0.90	0.83	0.82	0.83	0.85
	DMDI-1	0.32	0.41	0.37	0.36	0.36	0.35	0.37	0.32	0.33	0.38	0.37	0.34	0.34	0.35	0.36	0.34	0.36	0.35	0.33	0.33	0.33
	DMDI-2	0.35	0.40	0.35	0.35	0.31	0.30	0.36	0.37	0.37	0.39	0.38	0.34	0.39	0.39	0.39	0.40	0.40	0.38	0.39	0.39	0.40
	TMDI	0.85	0.68	0.72	0.84	0.78	0.75	0.76	0.82	0.81	0.81	0.87	0.81	0.81	0.84	0.85	0.82	0.82	0.80	0.85	0.83	0.82
	MDs/DMDs	5.84	0.22	1.32	1.20	1.27	1.31	1.34	1.32	1.20	1.26	1.20	1.24	1.13	1.15	1.19	1.15	1.14	1.26	1.15	1.10	1.08
	A/D	0.21	0.08	0.14	0.15	0.17	0.21	0.24	0.09	0.28	0.35	0.31	0.45	0.57	0.45	0.47	0.59	0.24	0.52	0.47	0.44	0.36
	MAs/MDs	0.23	0.84	0.74	0.87	1.11	1.32	1.35	1.74	1.60	1.26	1.44	1.49	1.85	1.50	1.42	1.73	0.96	1.55	1.55	1.48	1.32
	DMAAs/MDs	0.50	2.06	1.86	2.35	2.48	2.83	2.81	3.69	3.57	3.08	3.16	3.26	4.09	3.58	3.54	3.99	2.83	3.70	3.62	3.65	3.47
	DMAAs/DMDs	3.14	0.52	2.64	3.07	3.41	3.96	4.07	5.24	4.60	4.18	4.06	4.39	4.95	4.47	4.52	4.92	3.44	5.04	4.49	4.29	4.11
As/Ds	2.12	0.97	2.03	2.68	2.46	2.50	2.74	3.05	4.18	3.69	3.62	4.23	5.01	4.52	4.51	4.95	3.68	4.90	4.60	4.59	4.42	

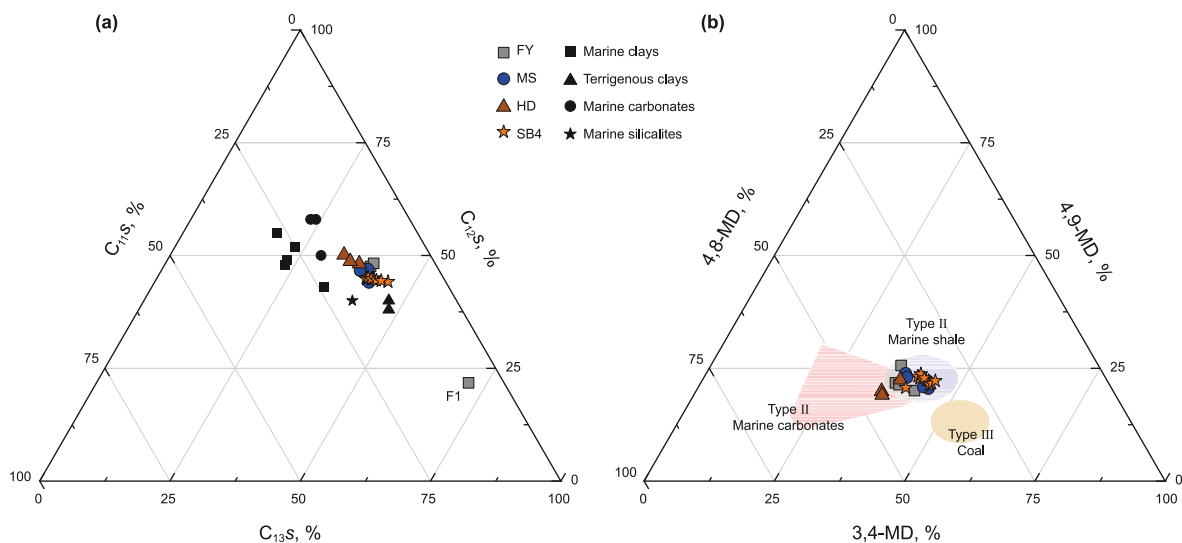


Fig. 5. Distribution of source-related diamondoids: (a) ternary plot of  $\sum C_{13S}-\sum C_{12S}-\sum C_{11S}$  (see Table S1 for explanation), the data points in black are from Gordadze (2008); (b) ternary plot of 3,4-MD, 4,9-MD, and 4,8-MD, the colored areas are from Schulz et al. (2001).

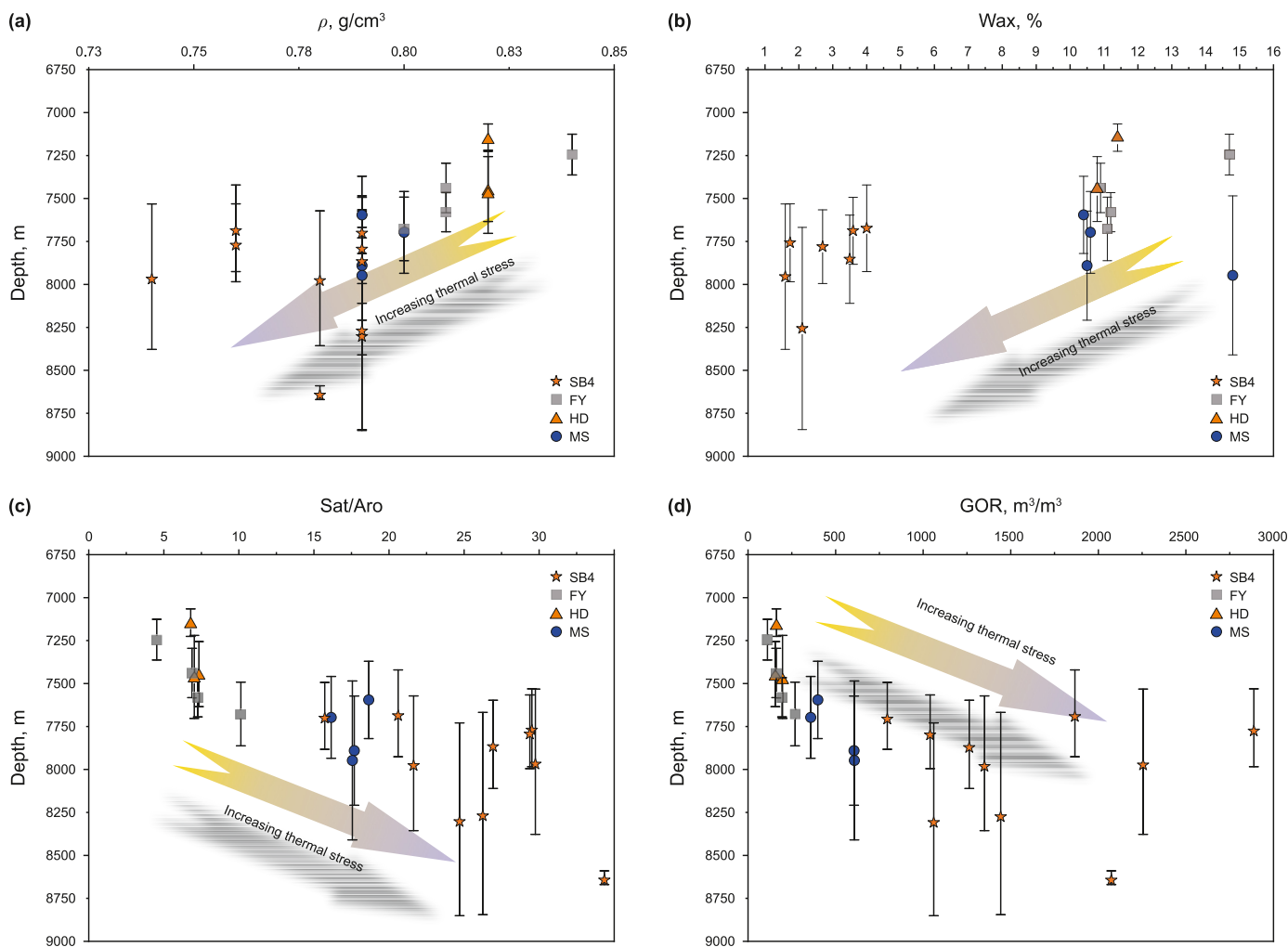


Fig. 6. (a) The correlation between depth (m) and density ( $\rho$ , g/cm<sup>3</sup>), (b) content of wax (%), (c) Sat/Aro, and (d) GOR (m<sup>3</sup>/m<sup>3</sup>), respectively. The arrows show the trend of increasing thermal stress. The depth of each sample is the average value of the depth range; the error bars indicate the depth range.

abundance of C<sub>0</sub> and C<sub>5</sub>-alkylated adamantanes declines. Notably, C<sub>2</sub>- and C<sub>3</sub>-alkylated adamantanes dominate, with C<sub>3</sub>-alkylated adamantanes exhibiting significant proportions. Increasing thermal stress correlates with heightened percentages of C<sub>2</sub>- and C<sub>3</sub>-alkylated adamantanes (Fang et al., 2013). Extracts from source rocks, particularly at >1.7% EasyR<sub>0</sub>, show elevated levels of C<sub>3</sub>- and C<sub>4</sub>-alkylated adamantanes, highlighting their enhanced thermal stability (Fang et al., 2015). Consequently, the presence of highly alkylated diamondoids (C<sub>2+</sub> alkylation) significantly varies with advancing maturity, underscoring their potential as indicators of thermal maturity.

From wells F2 to H3, C<sub>2</sub>-alkylated adamantanes exhibit relative percentages between 32% and 36%, whereas C<sub>3</sub>-alkylated adamantanes range from 24% to 27% (Fig. 7). In contrast, in MS and SB4 areas, these figures adjust to 29%–32% for C<sub>2</sub>-alkylated and 26%–29% for C<sub>3</sub>-alkylated adamantanes. Alkylated adamantanes in STGL oils show marked differentiation: for wells F3, H1, H2, and H3, percentages span 29%–33% for C<sub>0</sub>-unalkylated, 33%–36% for C<sub>1</sub>-alkylated, and 25%–28% for C<sub>2</sub>-alkylated adamantanes. In a comparative analysis, wells M2 to S10 report 16%–23%, 38%–41%, and 31%–37% for the same groups, respectively. These patterns underscore minimal variation in adamantane compounds yet a notable increase in C<sub>1</sub>- and C<sub>2</sub>-alkylated adamantanes correlating with maturity.

However, deviations exist. Well F1 shows a distinctive distribution with 53% C<sub>3</sub>-alkylated adamantanes, alongside notable quantities of C<sub>2</sub>- and C<sub>4</sub>-alkylated adamantanes, indicative of hydrothermal alterations. Here, C<sub>0</sub> adamantane are at a mere 11%, while C<sub>1</sub>-alkyladamantanes reach 73%. Conversely, well F2 reveals 17% C<sub>0</sub> adamantane and 65% C<sub>2</sub>-alkylated adamantanes, hinting at early losses of light hydrocarbons without subsequent recharging, reflected in the predominance of C<sub>2</sub>-alkylated forms. The distribution of both adamantanes and diamantanes in well F4 mirrors those observed in MS and SB4 areas, suggesting comparably higher maturity. Remarkably, well F1 registers an exceptional 52% of C<sub>0</sub>-unalkylated adamantane, pointing to intense charging by light hydrocarbons. Collectively, these findings illustrate a complex scenario of multiple charging in ultra-deep reservoirs within the STGL area.

In the STGL area, thermal stress predominantly affects the percentages of C<sub>1</sub>- and C<sub>2</sub>-alkylated adamantanes, whereas C<sub>3</sub>-

alkylated adamantanes are either unaffected or only slightly influenced. In contrast, the abundances of Ds and MDs compounds exhibit significant alterations. Ternary distributions of alkyl adamantanes and alkyl diamantanes display marked variability with maturity (Zheng et al., 2023). Notably, the relative percentages of 4-MD, 1-MD, and 3-MD demonstrate significant maturity variations (Fig. 8(a) and (b)), suggesting a %R<sub>0</sub> range between 1.5 and 2.5 for all samples (Zheng et al., 2023). However, the changes in the relative percentages of 1,4-DMA, 1,2-DMA, and 1,3-DMA present more subtle variations (Fig. 8(c)), while the TMAs compounds show minimal impact, maintaining a narrow range in their derived indices (Fig. 8(d)). Consequently, the crude oils in FY and HD areas exhibit low maturity, followed by the MS area with moderate maturity, and the SB4 area with high maturity.

### 5.2.3. Methyl-ethyl diamantane index (MEDI)

This part focuses on four indices including MAI, EAI, MDI, and MEDI (Table 3). The MEDI aims to reflect the differential thermal stability of methyl and ethyl diamantanes. MAI and MDI are commonly used indices to indicate maturity, with previous studies suggesting a strong correlation between MAI, MDI, and maturity (Chen et al., 1996; Zhang et al. 2000, 2019; Wei et al., 2007c; Fang et al., 2013; Jiang et al., 2019; Chai et al., 2020; Fu et al., 2023). However, Li et al. (2000) proposed MDI can be effective within the range of 0.9–2.0%R<sub>0</sub>. Walters et al. (2023) concluded that maturity indicators based on the ratio of alkyl substitutions at bridgehead versus secondary carbons are unreliable for the Eagle Ford condensate, as these indices show an inverse relationship at %R<sub>0</sub> ≤ 1.1 and demonstrate limited correlation at %R<sub>0</sub> ≥ 1.3. Similarly, we found a prevalent contradiction among many samples, characterized by high MAI and low MDI values (e.g. wells F1, S1 to S10) (Table 3). The values of MAI and MDI seem to deviate from the previously established notion of exhibiting a robust linear relationship with maturity.

A poor correlation between MAI and maturity was observed in the pyrolysis of crude oils (Fig. 9(a) and (b)). The R<sup>2</sup> values of MAI with Sat/Aro and GOR for crude oil samples from the STGL area were 0.46 and 0.28 respectively (Fig. 9(c) and (d)), indicating a weak correlation between MAI and maturity. In contrast, EAI consistently demonstrated a strong correlation across all experiments. Schulz et al. (2001) suggested EAI won't be influenced until

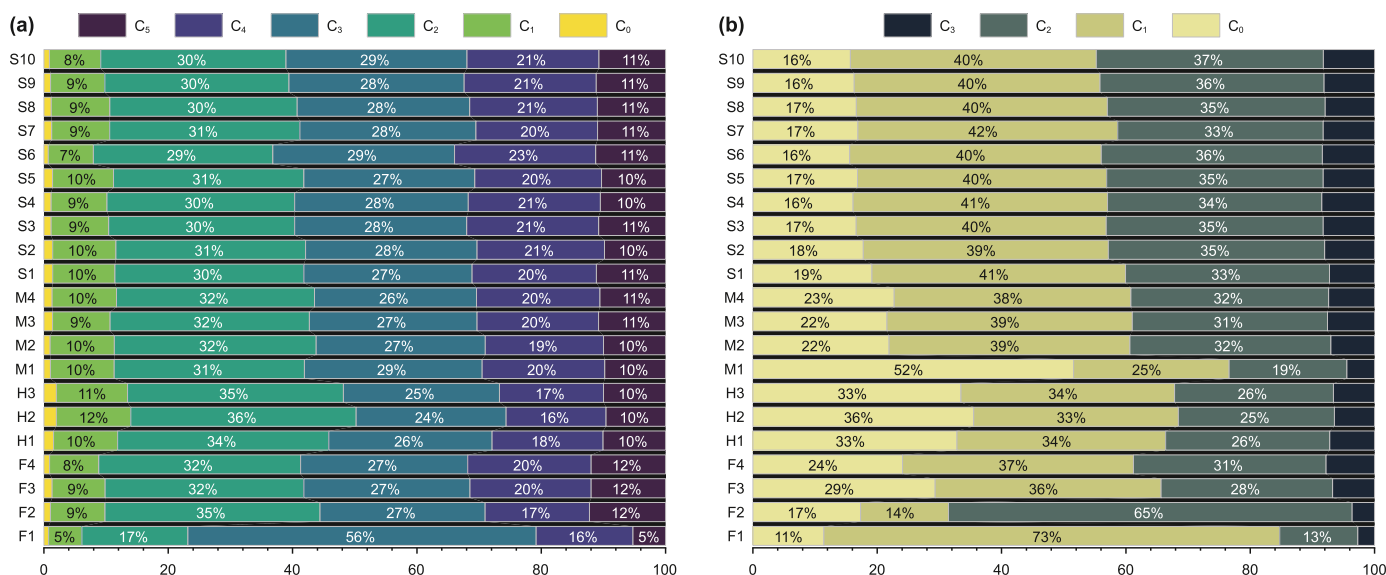
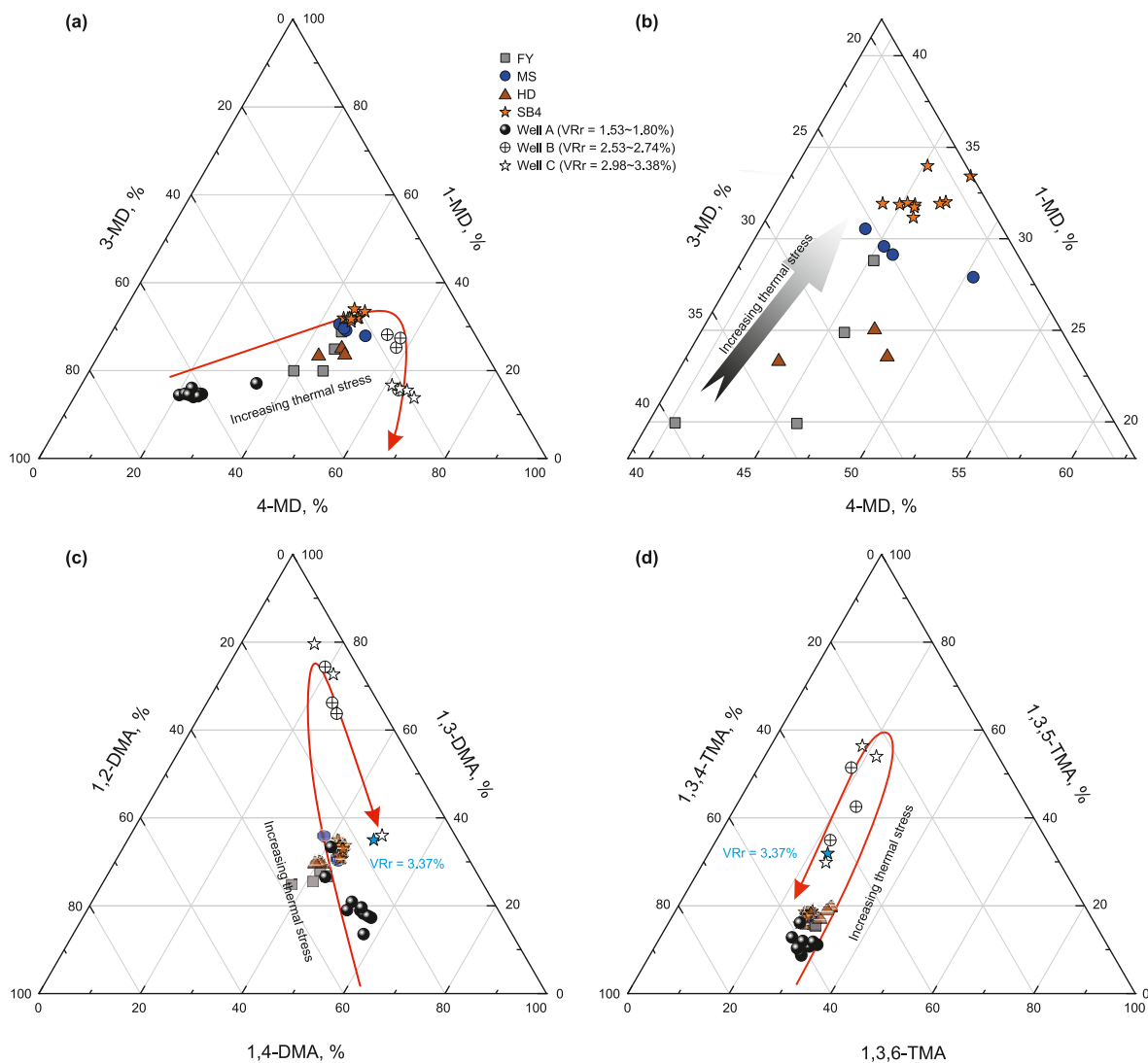


Fig. 7. (a) The relative percentage of C<sub>0</sub>-C<sub>5</sub>-alkylated adamantanes and (b) C<sub>0</sub>-C<sub>3</sub>-alkylated diamantanes.



**Fig. 8.** Ternary diagrams of alkyladamantanes and alkyldiamantanes in all oil samples. (b) is the enlarged image of (a). The data of wells A, B, and C are collected from Zheng et al. (2023). VRr: Vitritine reflectance, %. We speculated that the red arrow may indicate trends corresponding to increasing thermal stress.

the late gas generation stage. Zhang et al. (2005) reported that the EAI could serve as a maturity indicator. Subsequently, Pytlak et al. (2017) proposed that EAI is a maturity-dependent index with minor influence from source facies, as also evidenced by the application in Tarim basin (Li et al., 2018). Compared with MAI, the  $R^2$  coefficients between EAI and  $\text{Easy}R_o$  in the pyrolysis of crude oils reached 0.89 and 0.53, respectively (Fig. 9(e) and (f)) (Fang et al., 2012; Peng et al., 2022). The  $R^2$  values of EAI with Sat/Aro and GOR for STGL oils are up to 0.81 and 0.75, respectively (Fig. 9(g) and (h)). Therefore, EAI is an effective index to reveal the maturity of STGL crude oils.

The MDI exhibits a pronounced U-shaped trend during both kerogen and crude oil pyrolysis (Wei et al., 2007c; Fang et al., 2012; Li et al., 2015; Ma et al., 2020; Peng et al., 2022), initially decreasing and then increasing at  $<3.5\%$   $\text{Easy}R_o$  (Fig. 10), as also observed by Fang et al. (2016). The correlations between  $\%R_{\text{MDI}}$  and various maturity indicators such as  $\%R_{\text{MPI-1}}$  and  $\%R_{\text{MPR}}$  were found to be weak in studies of rock samples from the McArthur River Mine by Vinnichenko et al. (2021). Notably, MDI values are particularly high or low below  $1.0\%$   $\text{Easy}R_o$ , with the minimum value generally occurring around  $1.5\%$   $\text{Easy}R_o$ , though an outlier shows this

minimum at  $2.0\%$   $\text{Easy}R_o$  (Fig. 10(f)) (Peng et al., 2022). Above this level, MDI values rise with increasing  $\text{Easy}R_o$  (up to  $3.0\%$ ), decreasing to zero beyond this range due to the decomposition of diamondoids (Fig. 10(d)). MDI displays minimal correlation with GOR and Sat/Aro with an  $R^2$  of 0.06 (Fig. 11(a) and (b)). By comparison, MEDI shows a significant difference. In contrast, the MEDI shows a significantly strong correlation with Sat/Aro and GOR, achieving  $R^2$  values of 0.87 and 0.92, respectively, in exponential fits (Fig. 11(c) and (d)), indicating its potential as a promising indicator of maturity.

The correlation of MAI and MDI with thermal maturity is weaker than that of the EAI and MEDI due to multiple influencing factors. MAI is particularly susceptible to geological fractionation processes such as gas invasion, evaporation fractionation, migration fractionation and phase fractionation (Li et al., 2014; Gentzis and Carvajal-Ortiz, 2018; Zhu et al. 2019b, 2021; Spaak et al., 2020; Jiang et al., 2021; Wang et al., 2021; Qi et al. 2022, 2023; Fu et al., 2023; He et al., 2023b; Walters et al., 2023). Adamantanes, having a higher solubility in light hydrocarbons than diamantanes (Reiser et al., 1996), exhibit differential migration behaviors, significantly affecting their distribution in ultra-deep hydrocarbons. In open

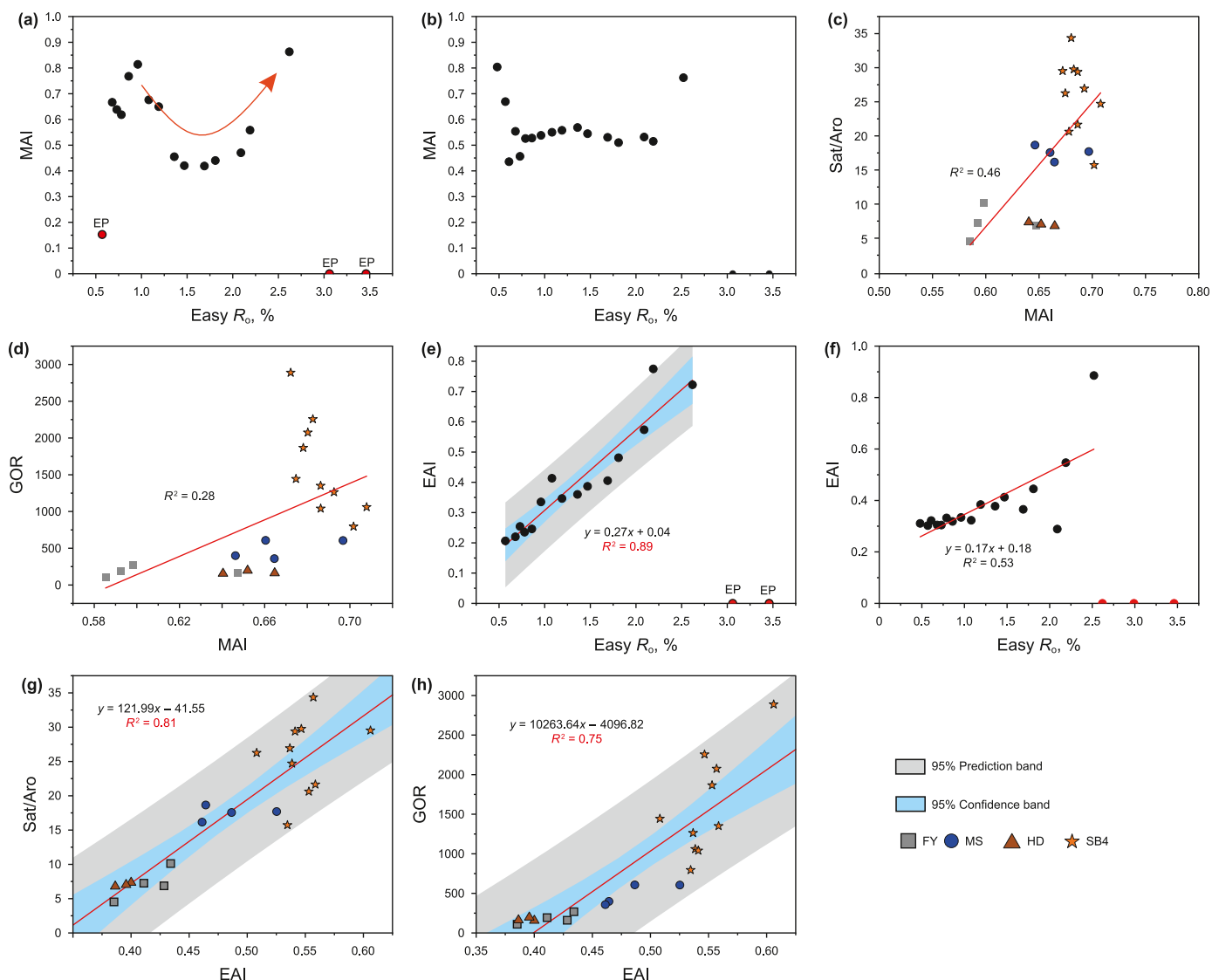


**Fig. 9.** Variations of MAI and EAI with increasing maturity. (a) and (e) show the distribution of diamondoids during anhydrous pyrolysis of crude oils, data from Fang et al. (2012); (b) and (f) show the distribution of diamondoids during hydrothermal pyrolysis of crude oils, data from Peng et al. (2022); (c) and (d) show the relationship of MAI, Sat/Aro and GOR; (g) and (h) show the relationship of EAI, Sat/Aro and GOR; EP: excluded points when fitting the curve; the red arrow indicates the inferred evolution trend.

thermal simulation systems, evaporation fractionation notably shifts MAI values, whereas EAI shows only minor fluctuations, and diamantane isomerization indices (MDI, DMDI-1, DMDI-2) remain largely stable. There is also evidence of preferential migration of adamantanes with the gasoline phase, affecting ratios such as A/MAs, A/1-MA, A/D, and MAs/DMAAs (Li et al., 2014). Conversely, in closed systems, MAI values are relatively consistent across gas and liquid phases despite pressure changes, while indices related to alkylated diamantanes consistently decrease in the gas phase (Chakhmakchev et al., 2017), indicating that pressure-driven phase fractionation has a limited impact on MAI. Extended periods of gas washing can result in higher MAI values in the gas phase. Additionally, the arrival of late-charged light hydrocarbons ( $C_1$ – $C_{12}$ ) of higher maturity can significantly alter the distribution of adamantanes in the original oil reservoir. However, alkyl-diamantanes show limited co-migration with these late-charged light hydrocarbons, suggesting a minimal impact on their distribution. For example, well F1 demonstrates elevated MAI and high percentages of TMAs and  $\sum C_{13}S$  due to abnormal influence of

hydrothermal activity, yet maintains a relatively low MEDI, indicative of the early-charged oils with lower maturity.

Mass chromatograms of representative samples elucidate that the relative abundance of 4-MD correlates positively with thermal maturity (Fig. 4). However, observations indicate complex interactions among 4-MD, 3-methyldiamantane (3-MD), and 1-methyldiamantane (1-MD), which deviate from simple linear correlations. Notably, 4-MD demonstrates enhanced thermal stability, while fluctuations in 1-MD provide a more sensitive indicator of incremental maturity changes. We proposed a three-stage model delineating the evolution of MDs and EDs across varying maturities. In the initial stage of low maturity, the distribution of diamantanes is primarily controlled by source facies, typically featuring a predominant abundance of 4-MD and lower initial concentrations of 1-MD, 3-MD, and EDs. This configuration results in elevated MDI and MEDI values. As maturity transitions to the intermediate stage, the abundance of 1-MD, 3-MD, and EDs progressively increases, leading to a reduction in both MDI and MEDI. In the final stage, characterized by high maturity, the less thermally stable 3-MD and EDs

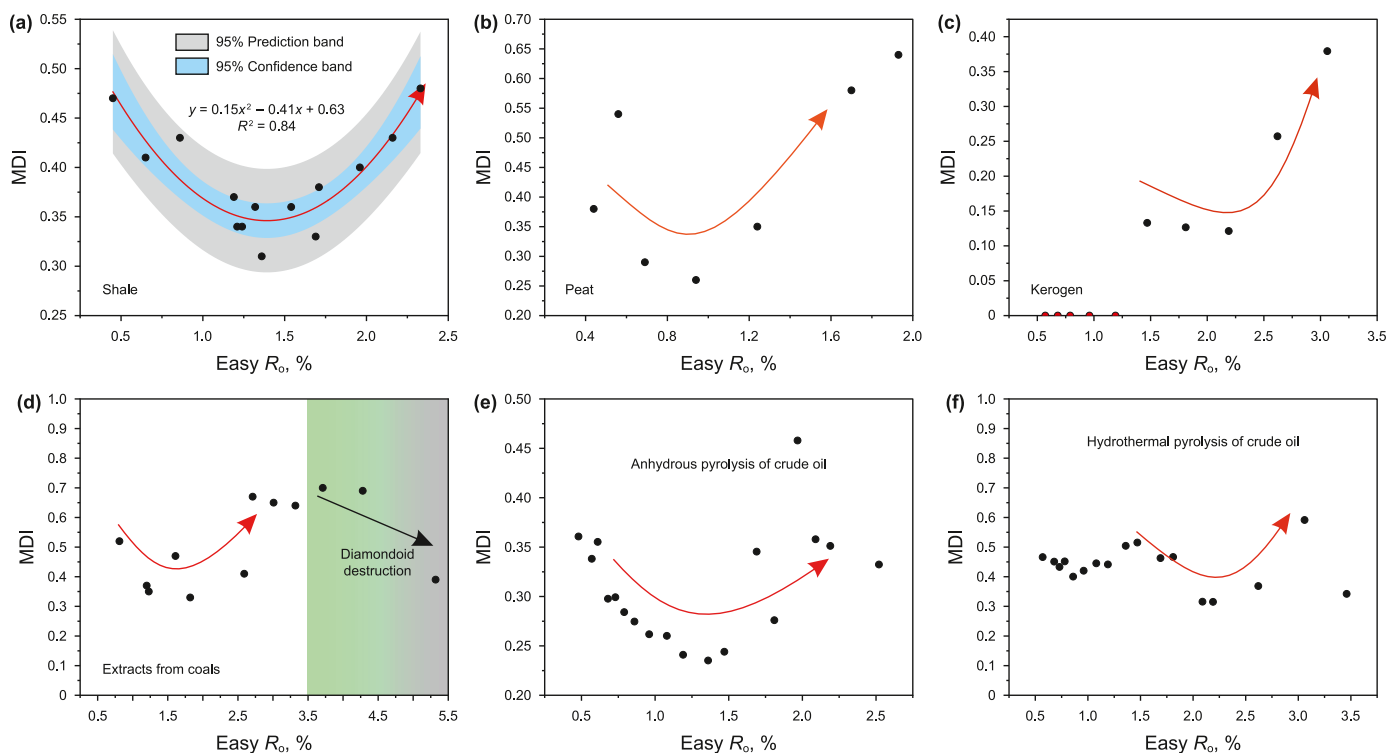


**Fig. 10.** The non-linear relationship between MDI and Easy $R_o$  (%) in a series of experiments. (a) and (b) represent the hydrous pyrolysis of shale and peat, respectively, data from [Wei et al. \(2007c\)](#); (c) the anhydrous pyrolysis of kerogen, data from [Li et al. \(2015\)](#); (d) the diamondoids in extracts of coals, data from [Ma et al. \(2020\)](#); (e) anhydrous pyrolysis of oil, data from [Fang et al. \(2012\)](#); (f) hydrothermal pyrolysis of crude oil, data from [Peng et al. \(2022\)](#). All curved arrows indicate the inferred evolution trend.

diminish, while 4-MD and 1-MD maintain higher relative abundances. Consequently, MEDI and the relative abundance of 1-MD notably increase, while the increase in abundance of 4-MD is comparatively marginal against the combined abundance of 1-MD and 3-MD.

Overall, The MDI primarily reflects variations in 4-MD, neglecting the coordinated dynamics among 1-MD, 3-MD, and 4-MD. In contrast, MEDI emerges as a robust indicator of maturity, effectively capturing the differential thermal stability between 4-MD and EDs. For instance, well F2 displays low MAI, EAI, and scarce 1-MD, collectively signifying minimal maturity consistent with the initial phase of the proposed model. The high MEDI mirrors these low maturity indications analogous to MDI trends ([Fig. 11](#)). Moreover, well F1 illustrates a distinct scenario where EAI is elevated while MEDI remains low, suggesting a pronounced influence of hydrothermal activity on EAI compared to MEDI.

#### 5.2.4. Other indices

This study reveals a specific range of response to maturity for DMAI-1 ([Fig. 11](#)(e) and (f)). DMAI-1 reflects the relatively low maturity in FY and HD areas, consistent with indicators like MEDI. However, an overlap in DMAI-1 values occurs in MS and SB4 regions, akin to observations in [Fig. 8](#)(c). To refine maturity assessment in hydrocarbon samples, our study utilized baseline metrics including Sat/Aro and GOR, conducting comprehensive correlation analysis with various maturity indices. Contrary to previous expectations, strong correlations were observed only with EAI, MEDI, TeMEAI, and As/Ds ([Fig. 12](#)), with ethyl diamondoid-derived indices (EAI, TeMEAI, MEDI) showing particularly robust positive correlation with Sat/Aro and GOR. This enhanced sensitivity to maturity may be attributed to the distinct chemical properties of ethyl groups compared to methyl groups. Ethyl groups, with their electron-donating nature and higher hydrogen atom content,

facilitate a denser electron cloud and lower bond dissociation energy. Under conditions of high thermal catalysis, this structural characteristic accelerates the loss of hydrogen atoms from ethyl groups, thereby diminishing the prevalence of ethyl diamondoids, a reaction that correlates closely with increased maturity levels.

The weak correlations among other indices could likely stem from their disparate maturity ranges. For example, although TMAI-1 and TMAI-2 are supposed to show strong correlations with maturity, the present maturity level appears to have little influence on the distribution of TMA, leading to minimal variation across all samples. The influence of source facies is also notable. [Walters et al. \(2023\)](#) proposed that the B/(B+S)A ratio in Eagle Ford shale samples can exceed 0.4. In contrast, all samples in this study consistently demonstrate values below 0.4, largely ascribed to variations in source facies. Due to the development of multiple deep and large faults in STGL area ([Deng et al., 2022](#); [Wang et al., 2023b](#)), the multiple charging and in-reservoir mixing also significantly influence the distribution of diamondoids. Furthermore, the intricate transformation mechanisms of diverse diamondoid compounds remain incompletely elucidated, such as the relative distribution among 1-MD, 3-MD, and 4-MD. Overall, this underscores the necessity of establishing the absolute value for indices in conjunction with specific geological contexts.

### 5.3. Multiple phase states of hydrocarbons

#### 5.3.1. Deep oil cracking under high thermal stress

The baseline concentration can be established by analyzing oil samples (uncracked, non-biodegraded, and non-fractionated) within the maturity window. Based on the determined baseline, the extent of oil cracking (EOC) can be quantified based on the concentration of 4+3-MD ([Dahl et al., 1999](#)). However, the baseline for estimating the EOC is controversial. For example, [Moldowan](#)

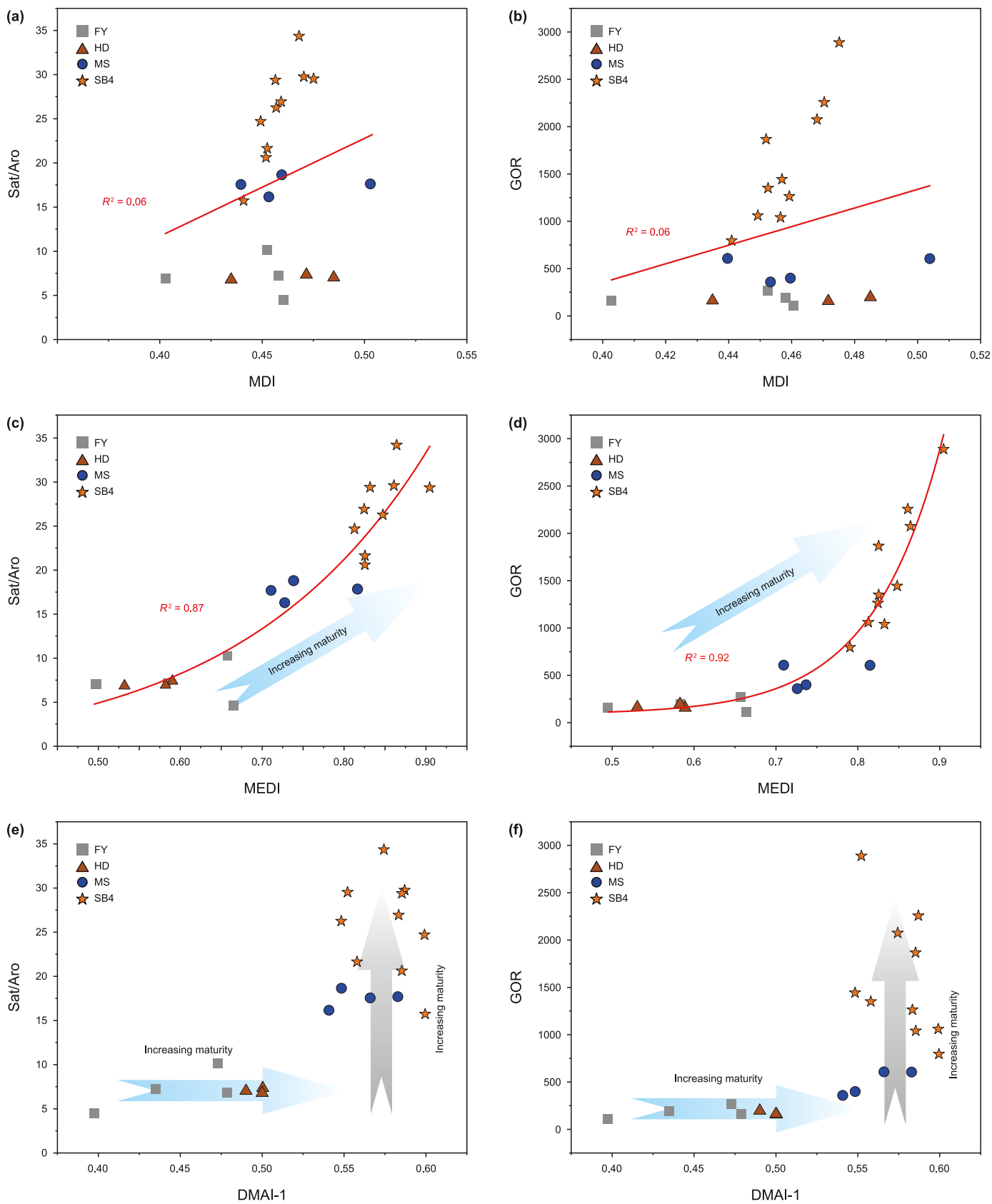


**Fig. 11.** Correlation between MDI, MEDI, DMAI-1 and Sat/Aro, GOR, respectively. (a) and (b): Linear fitting; (c) and (d): Exponential fitting; (e) and (f): Correlation between DMAI-1 and Sat/Aro, GOR, respectively. The red lines represent fitting function, the arrow indicates the increasing trend of thermal stress. It seems that DMAI-1 has reached the equilibrium value (or the ending value) among oil samples from MS and SB4 areas. GOR: gas-oil ratio,  $m^3/m^3$ .

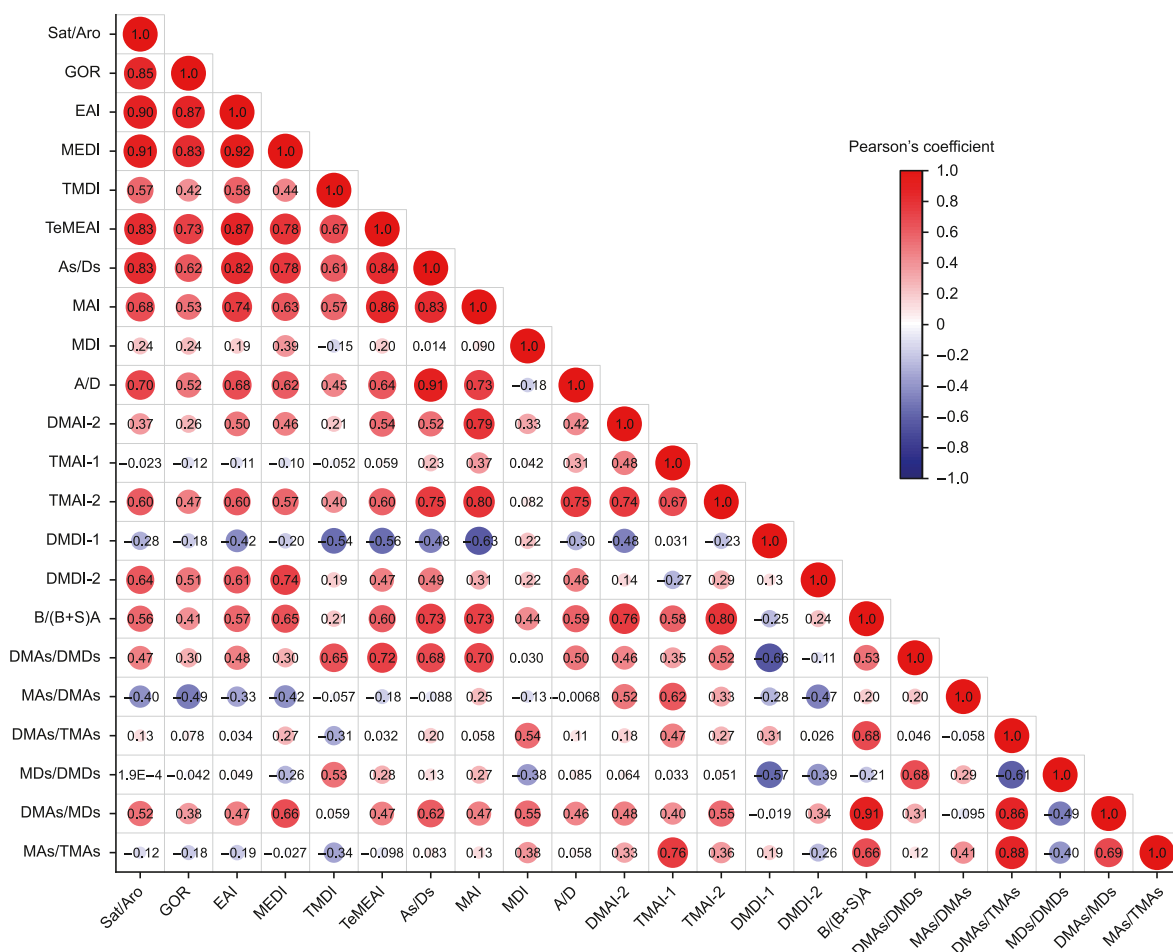


Fig. 12. Correlation map of various maturity-related indices. Note: All numbers indicate Pearson's coefficient.

et al. (2015) concluded that the baseline for oil cracking does not exceed 8 ppm, with a maximum of 10 ppm, while many researchers have determined that the baseline for oil cracking is far exceeding 10 ppm (e.g. Zhang et al., 2011; Fang et al., 2013; Ma et al., 2017; Li et al., 2018; Cheng et al., 2020; Qi et al., 2022; Chai and Chen, 2023). In reservoirs located near source rocks, such as shale oil reservoirs

where oils are retained within the source rocks themselves (Song et al., 2024), the continuous hydrocarbon supply from these source rocks may lead to a baseline that remains near zero. Conversely, for reservoirs situated far from the source rocks, the baseline is expected to be higher due to the mixture of low-maturity oils and high-maturity light hydrocarbons. The ultra-

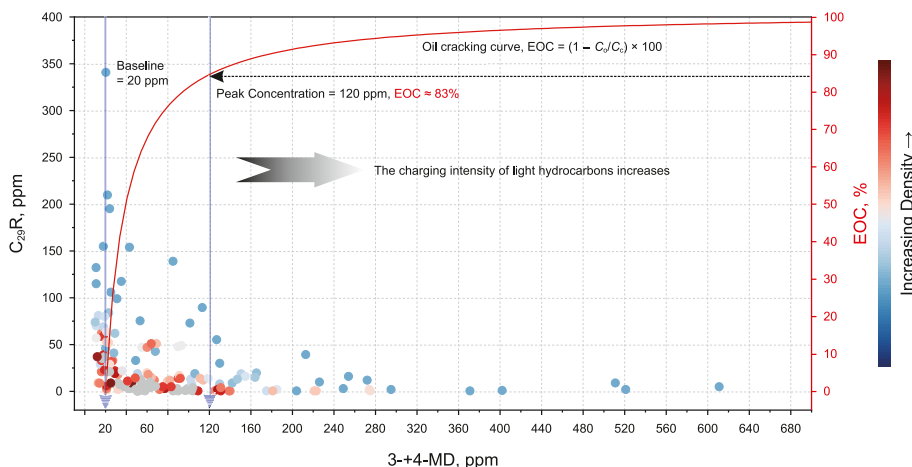


Fig. 13. Density plot of (3+4)- MD vs C<sub>29</sub>R, ppm. The bright color shows an increasing density of data. All data collected from previous studies, see Supplemental Table S3 for detailed information. The function of calculating the extent of oil cracking (EOC) is from Dahl et al. (1999), C<sub>0</sub> = 20 ppm.

deep reservoirs in Tarim Basin, being situated at a considerable distance from the source rocks, are supposed to exhibit higher baseline values.

Based on comprehensive data analysis, we propose establishing the baseline for ultra-deep crude oil cracking in the STGL area at approximately 20 ppm (Fig. 13). The function suggests that an estimated EOC of around 50% correlates with a 3-+4-MD concentration of 40 ppm. As the EOC approximates 83%, the peak concentration of 3-+4-MD reaches 120 ppm. Crucially, the accuracy of 3-+4-MD as a marker for EOC depends on the ppm of C<sub>29</sub>R nearing zero. Concentrations exceeding 120 ppm of 3-+4-MD are likely indicative of multiple charging events and in-reservoir mixing rather than straightforward oil cracking.

In FY and HD areas, the concentrations of 3-+4-MD remain below 50 ppm, signaling a lower EOC. Conversely, in the SB4 area, concentrations surpass this threshold (Fig. 14), hinting at origins from deeper reservoir cracking. Wang et al. (2023a) reported a 3-+4-MD concentration of 31 ppm at well MS1, from which we speculate a relatively high concentration of 3-+4-MD at wells in MS area. Ma and Qi (2023) noted lower concentrations ranging from 27.66 to 46.75 µg/g in wells SB44X, SB41X, and SB42X, while significantly higher concentrations (between 139.09 and 523.21 µg/g) were observed in wells SB41X-C and SB4, indicating the contribution of light hydrocarbons from deeper oil cracking, particularly in SB4, where the EOC is markedly higher.

### 5.3.2. Multiple charging and in-reservoir mixing

Zhang et al. (2005) proposed that the normal oils with a wide maturity range consist of multiple charges from various carbon numbers of hydrocarbons and in-reservoir mixing and the heavy oils with low maturity are considered as the residue oils with light fraction migrating away. Zhang et al. (2018) reported that the Hade-Yuke area underwent two stages of hydrocarbon charging, consisting of an early oil charge in the Late Hercynian and a later gas charge in the Llate Himalayan, respectively. Thus, secondary gas charging was responsible for the complex fluid character and multi-phase states of hydrocarbons. Similarly, the Tazhong area has also experienced multiple charging of oil and gas, which primarily accounted for the multiple phase states of petroleum reservoirs. In summary, the normal oils will be transformed into volatiles by substantial gas charging and subsequent geological fractionation processes (e.g. migration fractionation, evaporation fractionation, phase fractionation, TSR) will lead to the occurrence of various phase states including the black oils, condensates, and gas (Zhang et al., 2011; Huang et al., 2017; Chen et al., 2023; Fu et al., 2023; Li et al., 2023).

Wax precipitates out of the crude oil after the reservoir receives strong gas charging (Zhang et al., 2005). The high wax content

(>10%) observed in STGL area indicates significant gas charging. MAI is easily affected by light hydrocarbon charging, resulting in an increase in the original value. Contradictory MAI and MEDI values are strong indicators of the secondary charging of light hydrocarbons. For example, crude oils from the FY and HD areas are characterized by low MEDI, and high MAI, indicating the mixing of low-maturity oils and high-maturity light hydrocarbons. During the evaporation fractionation process, the A/D ratio of the condensates is greater than 1.0, while the A/D ratio of the light oil is less than 1.0 (Chakhmakhchev et al., 2017; He et al., 2023a). The A/D of all samples in this study is less than 1, suggesting the in-reservoir mixing of oil and gas without secondary fractionation by gas charging. Based on diamondoids indices, our study suggests that the arrival of the light hydrocarbon fraction had a significant impact on phase states of ultra-deep hydrocarbons compared with only considering the impact of gas. The low wax content in SB4 area indicates the oil maturity surpasses that of FY, HD, and MS areas, consistent with the lower wax content typically found in highly mature crude oil. Combined with the above discussion of maturity evaluation, the maturity of crude oils is low in FY and HD areas, moderate in MS area, and high in SB4 area. The in-reservoir mixing of crude oils and light hydrocarbons generated from source rock maturation leads to the formation of black oils in FY and HD areas. The volatile oils/condensate in MS area primarily result from the in-reservoir mixing of crude oils with moderate maturity and light hydrocarbons with high maturity, while condensates in SB4 primarily derive from kerogen maturation in late catagenesis, supplemented by light hydrocarbons produced through extensive oil cracking in deeper reservoirs. It is noteworthy that some of the light hydrocarbons in MS and SB4 areas originate from oil cracking in deep reservoirs which may exceed 9000 m.

## 6. Conclusions

Source-related diamondoids indicate that crude oils mainly come from marine siliceous shale. The bulk characteristics of Sat/Aro, GOR, and Density show the relative variation of maturities: low maturity in FY and HD areas, moderate maturity in MS area, and high maturity in SB4 area, respectively. We systematically report the thermal transformation of diamondoids in ultra-deep hydrocarbons. The percentage of C<sub>1</sub>- and C<sub>2</sub>-alkylated diamantanes will increase with increasing maturity, and hydrothermal activity may lead to an abnormal increase in the percentage of C<sub>3</sub>-alkylated adamantanes (e.g. well F1). The applications of commonly used maturity-related diamondoid indices should be cautious especially when the evaporation fractionation appears. MAI displays a modest correlation with maturity, attributed to the influence of late-charged light hydrocarbons. The MDI appears unreliable due to observed three-stage transformations with increasing maturity for both MDs and EDs. Despite the higher thermal stability of 4-MD, a more sensitive change in relative abundance with maturity for 1-MD among all MDs is observed. Ethyl diamondoids are less thermally stable and their derived indices can effectively indicate maturity. Overall, EAI, MEDI, DMAI-1, TeMEAI, and As/Ds exhibit robust correlations with maturity, with MEDI particularly recommended for high-maturity hydrocarbons.

The black oils in the FY and HD areas comprise mixtures of low-maturity oils with light hydrocarbons, predominantly sourced from the initial stages of source rock maturation, indicated by 3-+4-MD concentrations below 20 ppm. Conversely, in the MS area, volatile oils and condensates arise from a mixture of early-charged oils of moderate maturity and late-charged light hydrocarbons, products of both source rock maturation and deep reservoir oil cracking. In the SB4 area, condensates mainly stem from kerogen maturation during late catagenesis, augmented by light hydrocarbons partially

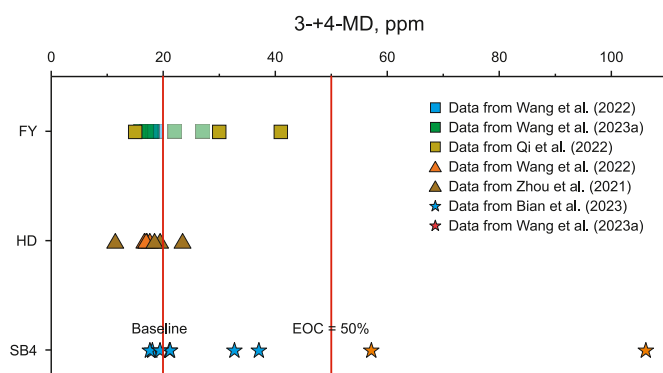


Fig. 14. The concentrations of (3-+4-) MD in FY, HD, and SB4 areas, ppm.

generated from extensive oil cracking in deeper reservoirs. Collectively, the phase states of ultra-deep oil reservoirs are controlled significantly by multiple charging and the in-reservoir mixing of light hydrocarbons and oils with various maturities.

### CRedit authorship contribution statement

**Bi-Qing Zhu:** Writing – review & editing, Writing – original draft, Visualization, Software, Methodology, Investigation, Formal analysis, Data curation, Conceptualization. **Quan-You Liu:** Writing – review & editing, Supervision, Resources, Funding acquisition. **Hui-Yuan Xu:** Writing – review & editing, Validation, Methodology, Formal analysis. **Dong-Ya Zhu:** Supervision, Resources. **Peng-Peng Li:** Resources. **Wei-Long Peng:** Resources. **Chi Zhang:** Software, Investigation, Conceptualization.

### Declaration of competing interest

The authors declare that they have no known competing financial interests or personal relationships that could have appeared to influence the work reported in this paper.

### Acknowledgments

This research was supported by the National Natural Science Foundation of China (Grant No. U20B6001, 41472108). The authors acknowledge the State Key Laboratory of Petroleum Resources and Engineering, China University of Petroleum (Beijing) for providing the experimental assistance. Two anonymous reviewers are thanked for their helpful comments and constructive feedback that much improved this manuscript.

### Appendix A. Supplementary data

Supplementary data to this article can be found online at <https://doi.org/10.1016/j.petsci.2025.02.017>.

### References

- Atwah, I., Mohammadi, S., Moldowan, J.M., Dahl, J., 2021. Episodic hydrocarbon charge in tight Mississippian reservoirs of Central Oklahoma, USA: insights from oil inclusion geochemistry. *Mar. Petrol. Geol.* 123, 104742. <https://doi.org/10.1016/j.marpetgeo.2020.104742>.
- Azevedo, D.A., Tamaqueira, J.B., Dias, J.C.M., Carmo, A.P.B., Landau, L., Gonçalves, F.T.T., 2008. Multivariate statistical analysis of diamondoid and biomarker data from Brazilian basin oil samples. *Fuel* 87, 2122–2130. <https://doi.org/10.1016/j.fuel.2007.11.005>.
- Bian, J.J., Hou, D.J., Cui, Y.W., Zhu, X.X., 2023. Geochemical characteristics and origin of the ultra-deep hydrocarbons from the Shunbei Oilfield in the Tarim Basin, China: insight from molecular biomarkers and carbon isotope geochemistry. *Mar. Petrol. Geol.* 158, 106542. <https://doi.org/10.1016/j.marpetgeo.2023.106542>.
- Boente, C., Márquez, G., Marín, P., Romero, E., Rodrigues, C.F.A., Guzmán, M.A., 2020. Classical biomarker and quantitative extended diamondoid analysis fingerprints for crude oils from deepwater developments in Block 17, Lower Congo Basin, Angola. *Int. J. Environ. Res. Publ. Health* 17 (19), 7204. <https://doi.org/10.3390/ijerph17197204>.
- Cai, C.F., Zhang, C.M., Worden, R.H., Wang, T.K., Li, H.X., Jiang, L., Huang, S.Y., Zhang, B.S., 2015. Application of sulfur and carbon isotopes to oil–source rock correlation: a case study from the Tazhong area, Tarim Basin, China. *Org. Geochem.* 83–84, 140–152. <https://doi.org/10.1016/j.orggeochem.2015.03.012>.
- Chai, Z., Chen, Z.H., 2023. Biomarkers, light hydrocarbons, and diamondoids of petroleum in deep reservoirs of the southeast Tabei Uplift, Tarim Basin: implication for its origin, alteration, and charging direction. *Mar. Petrol. Geol.* 147, 106019. <https://doi.org/10.1016/j.marpetgeo.2022.106019>.
- Chai, Z., Chen, Z.H., Liu, H., Cao, Z.C., Cheng, B., Wu, Z.P., Qu, J.X., 2020. Light hydrocarbons and diamondoids of light oils in deep reservoirs of Shuntuoguole Low Uplift, Tarim Basin: implication for the evaluation on thermal maturity, secondary alteration and source characteristics. *Mar. Petrol. Geol.* 117, 104388. <https://doi.org/10.1016/j.marpetgeo.2020.104388>.
- Chakhmakchev, A., Sanderson, J., Pearson, C., Davidson, N., 2017. Compositional changes of diamondoid distributions caused by simulated evaporative fractionation. *Org. Geochem.* 113, 224–228. <https://doi.org/10.1016/j.orggeochem.2017.06.016>.
- Chang, X.C., Wang, T.G., Li, Q.M., Ou, G.X., 2013. Charging of ordovician reservoirs in the halahatang depression (Tarim Basin, NW China) determined by oil geochemistry. *J. Petrol. Geol.* 36, 383–398. <https://doi.org/10.1111/jpg.12562>.
- Chang, X.C., Liu, X.M., Shi, B.B., Liu, T.J., Xu, Y.D., Liu, Z.Q., Chen, G., Zhang, P.F., 2022. Biodegradation levels of oils from the Chepaizi Uplift, Junggar Basin (NW China) evaluated by a full-range biodegradation index as constrained by adamantane, diamantane homologs and carboxylic acids. *Mar. Petrol. Geol.* 146, 105939. <https://doi.org/10.1016/j.marpetgeo.2022.105939>.
- Chen, C., Zhang, X.T., Peng, G.R., Long, Z.L., Liu, B.J., Wang, X.D., Zhai, P.Q., Zhang, B., 2023. Controlling factors on the charging process of oil and gas in the eastern main sub-sag of the baiyun sag, zhujiang river (pearl river) mouth basin. *Acta Oceanol. Sin.* 42, 189–200. <https://doi.org/10.1007/s13131-022-2140-z>.
- Chen, J.H., Fu, J.M., Sheng, G.Y., Liu, D.H., Zhang, J.J., 1996. Diamondoid hydrocarbon ratios: novel maturity indices for highly mature crude oils. *Org. Geochem.* 25, 179–190. [https://doi.org/10.1016/S0146-6380\(96\)00125-8](https://doi.org/10.1016/S0146-6380(96)00125-8).
- Chen, Z.H., Wang, T.G., Li, M.J., Yang, F.L., Cheng, B., 2018. Biomarker geochemistry of crude oils and Lower Paleozoic source rocks in the Tarim Basin, western China: an oil-source rock correlation study. *Mar. Petrol. Geol.* 96, 94–112. <https://doi.org/10.1016/j.marpetgeo.2018.05.023>.
- Chen, Z.H., Chai, Z., Cheng, B., Liu, H., Cao, Y.C., Cao, Z.C., Qu, J.X., 2021. Geochemistry of high-maturity crude oil and gas from deep reservoirs and their geological significance: a case study on Shuntuoguole low uplift, Tarim Basin, western China. *AAPG (Am. Assoc. Pet. Geol.) Bull.* 105, 65–107. <https://doi.org/10.1306/07072019015>.
- Cheng, B., Wang, T.G., Huang, H.P., Wang, G.L., Simoneit, B.R.T., 2015. Ratios of low molecular weight alkylbenzenes (C<sub>0</sub>–C<sub>4</sub>) in Chinese crude oils as indicators of maturity and depositional environment. *Org. Geochem.* 88, 78–90. <https://doi.org/10.1016/j.orggeochem.2015.08.008>.
- Cheng, B., Liu, H., Cao, Z.C., Wu, X., Chen, Z.H., 2020. Origin of deep oil accumulations in carbonate reservoirs within the north Tarim Basin: insights from molecular and isotopic compositions. *Org. Geochem.* 139, 103931. <https://doi.org/10.1016/j.orggeochem.2019.103931>.
- Clark, T., Knox, T.M., McKervey, M.A., Mackle, H., Rooney, J.J., 1979. Thermochemistry of bridged-ring substances. Enthalpies of formation of some diamondoid hydrocarbons and of perhydroquinacene. Comparisons with data from empirical force field calculations. *J. Am. Chem. Soc.* 101, 2404–2410. <https://doi.org/10.1021/ja00503a028>.
- Claypool, G.E., Mancini, E.A., 1989. Geochemical relationships of petroleum in mesozoic reservoirs to carbonate source rocks of Jurassic Smackover Formation, Southwestern Alabama. *AAPG (Am. Assoc. Pet. Geol.) Bull.* 73, 904–924. <https://doi.org/10.1306/44B4A28F-170A-11D7-8645000102C1865D>.
- Dahl, J.E., Liu, S.G., Carlson, R.M.K., 2003. Isolation and structure of higher diamondoids, nanometer-sized diamond molecules. *Science* 299, 96–99. <https://doi.org/10.1126/science.1078239>.
- Dahl, J.E., Moldowan, J.M., Peters, K.E., Claypool, G.E., Rooney, M.A., Michael, G.E., Mello, M.R., Kohnen, M.L., 1999. Diamondoid hydrocarbons as indicators of natural oil cracking. *Nature* 399, 54–57. <https://doi.org/10.1038/19953>.
- de Araujo, P.L.B., Mansoori, G.A., de Araujo, E.S., 2012. Diamondoids: occurrence in fossil fuels, applications in petroleum exploration and fouling in petroleum production. A review paper. *Int. J. Oil Gas Coal Technol.* 5, 316–367. <https://doi.org/10.1504/IJOGCT.2012.048981>.
- Deng, S., Zhao, R., Kong, Q.F., Li, Y.T., Li, B., 2022. Two distinct strike-slip fault networks in the Shunbei area and its surroundings, Tarim Basin: hydrocarbon accumulation, distribution, and controlling factors. *AAPG (Am. Assoc. Pet. Geol.) Bull.* 106, 77–102. <https://doi.org/10.1306/07202119113>.
- Esegbue, O., Jones, D.M., van Bergen, P.F., Kolonic, S., 2020. Quantitative diamondoid analysis indicates oil cosourcing from a deep petroleum system onshore Niger Delta Basin. *AAPG (Am. Assoc. Pet. Geol.) Bull.* 104, 1231–1259. <https://doi.org/10.1306/0122201618217407>.
- Fang, C.C., Xiong, Y.Q., Liang, Q.Y., Li, Y., 2012. Variation in abundance and distribution of diamondoids during oil cracking. *Org. Geochem.* 47, 1–8. <https://doi.org/10.1016/j.orggeochem.2012.03.003>.
- Fang, C.C., Wu, W., Liu, D., Liu, J.Z., 2016. Evolution characteristics and application of diamondoids in coal measures. *Journal of Natural Gas Geoscience* 1, 93–99. <https://doi.org/10.1016/j.jnggs.2016.02.001>.
- Fang, C.C., Xiong, Y.Q., Li, Y., Chen, Y., Tang, Y.J., 2015. Generation and evolution of diamondoids in source rock. *Mar. Petrol. Geol.* 67, 197–203. <https://doi.org/10.1016/j.marpetgeo.2015.05.018>.
- Fang, C.C., Xiong, Y.Q., Li, Y., Chen, Y., Liu, J.Z., Zhang, H.Z., Adedosu, T.A., Peng, P.A., 2013. The origin and evolution of adamantanes and diamantanes in petroleum. *Geochim. Cosmochim. Acta* 120, 109–120. <https://doi.org/10.1016/j.gca.2013.06.027>.
- Forkner, R., Fildani, A., Ochoa, J., Moldowan, J.M., 2021. Linking source rock to expelled hydrocarbons using diamondoids: an integrated approach from the Northern Gulf of Mexico. *J. Petrol. Sci. Eng.* 196, 108015. <https://doi.org/10.1016/j.petrol.2020.108015>.
- Fu, J., Li, M.J., Sun, Y.G., Li, Y.C., Yang, Y.C., Lu, X.L., Lai, G.T., 2023. Thermal maturity of crude oils in the Baiyun sag, Pearl River Mouth basin, South China Sea: insights from biomarkers, aromatic hydrocarbon and adamantane compounds. *Mar. Petrol. Geol.* 155, 106353. <https://doi.org/10.1016/j.marpetgeo.2023.106353>.
- Gentzis, T., Carvajal-Ortiz, H., 2018. Comparative study of conventional maturity proxies with the methylidiamondoid ratio: examples from West Texas, the Middle East, and northern South America. *Int. J. Coal Geol.* 197, 115–125. <https://doi.org/10.1016/j.coal.2018.08.009>.

- Gordadze, G.N., 2008. Geochemistry of cage hydrocarbons. *Petrol. Chem.* 48, 241–253. <https://doi.org/10.1134/S0965544108040014>.
- Grice, K., Alexander, R., Kagi, R.I., 2000. Diamondoid hydrocarbon ratios as indicators of biodegradation in Australian crude oils. *Org. Geochem.* 31, 67–73. [https://doi.org/10.1016/S0146-6380\(99\)00137-0](https://doi.org/10.1016/S0146-6380(99)00137-0).
- Hackley, P.C., Parris, T.M., Eble, C.F., Greb, S.F., Harris, D.C., 2021. Oil–source correlation studies in the shallow Berea Sandstone petroleum system, eastern Kentucky. *AAPG (Am. Assoc. Pet. Geol.) Bull.* 105, 517–542. <https://doi.org/10.1306/08192019077>.
- Han, J.F., Wang, P., Zhu, G.Y., Zhang, Y.T., Li, S.Y., Xie, Z., 2023. Petroleum geology and distribution law of high efficiency areas in ultra-deep kiloton wells in Tarim Basin. *Nat. Gas Geosci.* 34, 735–748 (in Chinese).
- Hanson, A.D., Ritts, B.D., Moldowan, J.M., 2007. Organic geochemistry of oil and source rock strata of the Ordos Basin, north-central China. *AAPG (Am. Assoc. Pet. Geol.) Bull.* 91, 1273–1293. <https://doi.org/10.1306/05040704131>.
- Hanson, A.D., Zhang, S.C., Moldowan, J.M., Liang, D.G., Zhang, B.M., 2000. Molecular organic geochemistry of the Tarim Basin, northwest China. *AAPG (Am. Assoc. Pet. Geol.) Bull.* 84, 1109–1128. <https://doi.org/10.1306/A9673C52-1738-11D7-8645000102C1865D>.
- He, J.H., Wang, T.G., Tang, Y.J., Zhang, D.L., Zhang, T.L., Diao, H., Liu, B., Hu, Y., 2023a. Geochemical characteristics and gas-washing accumulation mechanism of hydrocarbon from the xihu sag, east China sea basin. *Geoenergy Science and Engineering* 224, 211639. <https://doi.org/10.1016/j.geoen.2023.211639>.
- He, T.H., Li, W.H., Lu, S.F., Pan, W.Q., Ying, J.F., Zhu, P.F., Yang, E.Q., Wang, X.Z., Zhang, B.S., Sun, D.Q., 2022. Mechanism and geological significance of anomalous negative  $\delta^{13}\text{C}$ kerogen in the lower cambrian, NW Tarim Basin, China. *J. Petrol. Sci. Eng.* 208, 109384. <https://doi.org/10.1016/j.petrol.2021.109384>.
- He, T.H., Zeng, Q.H., Lu, S.F., Li, W.H., Li, M.Q., Wen, Z.G., Yang, E.Q., Jing, T.T., Ying, J.F., Zhu, P.F., Wang, X.Z., Pan, W.Q., Zhang, B.S., Chen, Z.H., 2023b. Aryl isoprenoids from the lower paleozoic in the Tarim Basin, NW China: insight into deep ancient hydrocarbon exploration. *Geoenergy Science and Engineering* 225, 211666. <https://doi.org/10.1016/j.geoen.2023.211666>.
- Huang, H.P., Zhang, S.C., Su, J., 2016. Palaeozoic oil–source correlation in the Tarim Basin, NW China: a review. *Org. Geochem.* 94, 32–46. <https://doi.org/10.1016/j.orggeochem.2016.01.008>.
- Huang, H.P., Zhang, S.C., Gu, Y., Su, J., 2017. Impacts of source input and secondary alteration on the extended tricyclic terpane ratio: a case study from Palaeozoic sourced oils and condensates in the Tarim Basin, NW China. *Org. Geochem.* 112, 158–169. <https://doi.org/10.1016/j.orggeochem.2017.07.012>.
- Huang, W.Y., Zhang, H.Z., Xiao, Z.Y., Yu, S., Pan, C.C., 2022. Generation, expulsion and accumulation of diamondoids, aromatic components and gaseous hydrocarbons for gas fields in Kuqa Depression of the Tarim Basin, NW China. *Mar. Petrol. Geol.* 145, 105893. <https://doi.org/10.1016/j.marpetgeo.2022.105893>.
- Jia, W.L., Peng, P.A., Yu, C.L., Xiao, Z.Y., 2007. Source of 1,2,3,4-tetramethylbenzene in asphaltenes from the Tarim Basin. *J. Asian Earth Sci.* 30, 591–598. <https://doi.org/10.1016/j.jseae.2006.09.003>.
- Jia, W.L., Xiao, Z.Y., Yu, C.L., Peng, P.A., 2010. Molecular and isotopic compositions of bitumens in Silurian tar sands from the Tarim Basin, NW China: characterizing biodegradation and hydrocarbon charging in an old composite basin. *Mar. Petrol. Geol.* 27, 13–25. <https://doi.org/10.1016/j.marpetgeo.2009.09.003>.
- Jiang, W.M., Li, Y., Xiong, Y.Q., 2018. The effect of organic matter type on formation and evolution of diamondoids. *Mar. Petrol. Geol.* 89, 714–720. <https://doi.org/10.1016/j.marpetgeo.2017.11.003>.
- Jiang, W.M., Li, Y., Xiong, Y.Q., 2019. Source and thermal maturity of crude oils in the Junggar Basin in northwest China determined from the concentration and distribution of diamondoids. *Org. Geochem.* 128, 148–160. <https://doi.org/10.1016/j.orggeochem.2019.01.004>.
- Jiang, W.M., Li, Y., Fang, C.C., Yu, Z.Q., Xiong, Y.Q., 2021. Diamondoids in petroleum: their potential as source and maturity indicators. *Org. Geochem.* 160, 104298. <https://doi.org/10.1016/j.orggeochem.2021.104298>.
- Killops, S., Killops, V., 2004. Long-term fate of organic matter in the geosphere. *Introduction to Organic Geochemistry* 117–165. <https://doi.org/10.1002/9781118697214.ch4>.
- Li, F., Lü, X.X., Zhu, G.Y., Chen, J.F., Wang, R., Wu, Z.H., He, T., Xue, N., 2023. Formation and preservation of ultra-deep liquid petroleum in the Ordovician sedimentary succession in Tarim Basin during the neotectonic phase. *J. Asian Earth Sci.* 250, 105645. <https://doi.org/10.1016/j.jseae.2023.105645>.
- Li, J.G., Paul, P., Cui, M.Z., 2000. Methyl diamantane index (MDI) as a maturity parameter for Lower Palaeozoic carbonate rocks at high maturity and over-maturity. *Org. Geochem.* 31, 267–272. [https://doi.org/10.1016/S0146-6380\(00\)00016-4](https://doi.org/10.1016/S0146-6380(00)00016-4).
- Li, Y., Xiong, Y.Q., Chen, Y., Tang, Y.J., 2014. The effect of evaporation on the concentration and distribution of diamondoids in oils. *Org. Geochem.* 69, 88–97. <https://doi.org/10.1016/j.orggeochem.2014.02.007>.
- Li, Y., Chen, Y., Xiong, Y.Q., Wang, X.T., Fang, C.C., Zhang, L., Li, J.H., 2015. Origin of adamantanes and diamantanes in marine source rock. *Energy Fuels* 29, 8188–8194. <https://doi.org/10.1021/acs.energyfuels.5b01993>.
- Li, Y., Xiong, Y.Q., Liang, Q.Y., Fang, C.C., Chen, Y., Wang, X.T., Liao, Z.W., Peng, P.A., 2018. The application of diamondoid indices in the Tarim oils. *AAPG (Am. Assoc. Pet. Geol.) Bull.* 102, 267–291. <https://doi.org/10.1306/0424171518217073>.
- Liang, Q.Y., Xiong, Y.Q., Fang, C.C., Li, Y., 2012. Quantitative analysis of diamondoids in crude oils using gas chromatography–triple quadrupole mass spectrometry. *Org. Geochem.* 43, 83–91. <https://doi.org/10.1016/j.orggeochem.2011.10.008>.
- Ma, A.L., 2016. Kinetics of oil-cracking for different types of marine oils from Tahe Oilfield, Tarim Basin, NW China. *Journal of Natural Gas Geoscience* 1, 35–43. <https://doi.org/10.1016/j.jnggs.2016.03.001>.
- Ma, A.L., Qi, L.X., 2023. Geochemical characteristics of oil and gas and difference in fluid phase in the ultra-deep Ordovician reservoirs from No.4 fault of north Shuntuoguole area of Tarim Basin, NW China. *Earth Sci. Front.* 30, 247–262. <https://doi.org/10.13745/j.esf.sf.2023.2.21> (in Chinese).
- Ma, A.L., He, Z.L., Yun, L., Wu, X., Qiu, N.S., Chang, J., Lin, H.X., Cao, Z.C., Zhu, X.X., You, D.H., 2021a. The geochemical characteristics and origin of Ordovician ultra-deep natural gas in the North Shuntuoguole area, Tarim Basin, NW China. *Journal of Natural Gas Geoscience* 6, 289–300. <https://doi.org/10.1016/j.jnggs.2021.09.004>.
- Ma, A.L., Jin, Z.J., Zhu, C.S., Bai, Z.R., 2017. Cracking and thermal maturity of ordovician oils from tahe oilfield, Tarim Basin, NW China. *Journal of Natural Gas Geoscience* 2, 239–252. <https://doi.org/10.1016/j.jnggs.2017.12.001>.
- Ma, A.L., Jin, Z.J., Yan, J.F., Mi, J.K., Li, J.H., 2020. Distribution and evolution of diamondoids in coals. *Acta Pet. Sin.* 41, 796–808 (in Chinese).
- Ma, A.L., Lin, H.X., Yun, L., Cao, Z.C., Zhu, X.X., Li, W.P., Wu, X., 2021b. Diamondoids in oils from the ultra-deep ordovician in the north Shuntuoguole area in the Tarim Basin, NW China. *Journal of Natural Gas Geoscience* 6, 89–99. <https://doi.org/10.1016/j.jnggs.2021.05.001>.
- Ma, Y.S., Cai, X.Y., Yun, L., Li, Z.J., Li, H.L., Deng, S., Zhao, P.R., 2022. Practice and theoretical and technical progress in exploration and development of Shunbei ultra-deep carbonate oil and gas field, Tarim Basin, NW China. *Petrol. Explor. Dev.* 49, 1–20. [https://doi.org/10.1016/S1876-3804\(22\)60001-6](https://doi.org/10.1016/S1876-3804(22)60001-6).
- Mei, M., Bissada, K.K., Malloy, T.B., Darnell, L.M., Liu, Z.F., 2018. Origin of condensates and natural gases in the Almond Formation reservoirs in southwestern Wyoming, USA. *Org. Geochem.* 124, 164–179. <https://doi.org/10.1016/j.orggeochem.2018.07.007>.
- Meng, B.K., Song, D.F., Chen, Y., Shi, S.B., 2024. Distribution and geochemical significance of alkylbenzenes for crude oil with different depositional environments and thermal maturities. *Pet. Sci.* 21, 777–790. <https://doi.org/10.1016/j.petsci.2023.10.030>.
- Moldowan, J.M., Dahl, J., Zinniker, D., Barbanti, S.M., 2015. Underutilized advanced geochemical technologies for oil and gas exploration and production-1. The diamondoids. *J. Petrol. Sci. Eng.* 126, 87–96. <https://doi.org/10.1016/j.petrol.2014.11.010>.
- Pang, X.Q., Jia, C.Z., Pang, H., Yang, H.J., 2018. Destruction of hydrocarbon reservoirs due to tectonic modifications: conceptual models and quantitative evaluation on the Tarim Basin, China. *Mar. Petrol. Geol.* 91, 401–421. <https://doi.org/10.1016/j.marpetgeo.2018.01.028>.
- Peng, W.L., Deng, S., Zhang, J.B., Huang, C., Qiu, H.B., Li, Y., Liu, Y.Q., Liu, D.W., 2024. Genetic mechanism and main controlling factors of deep marine condensate reservoirs: a case study of the Shunbei No.4 fault zone in Tarim Basin, NW China. *Nat. Gas Geosci.* 35, 838–850.
- Peng, Y.Y., Cai, C.F., Fang, C.C., Wu, L.L., Liu, J.Z., Sun, P., Liu, D.W., 2022. Diamondoids and thiadiamondoids generated from hydrothermal pyrolysis of crude oil and TSR experiments. *Sci. Rep.* 12, 196. <https://doi.org/10.1038/s41598-021-04270-z>.
- Pytlak, Ł., Kowalski, A., Gross, D., Sachsenhofer, R.F., 2017. Composition of diamondoids in oil samples from the Alpine foreland basin, Austria: potential as indices of source rock facies, maturity and biodegradation. *J. Petrol. Geol.* 40, 153–171. <https://doi.org/10.1111/jpg.12670>.
- Qi, L.X., 2016. Oil and gas breakthrough in ultra-deep Ordovician carbonate formations in Shuntuoguole uplift, Tarim Basin. *China Petroleum Exploration* 21, 38–51 (in Chinese).
- Qi, Y., Sun, P., Cai, C.F., Wang, D.W., Peng, Y.Y., 2022. Phase fractionation controlling regional distribution of diamondoids: a case study from the Halahatang oil field, Tarim Basin, China. *Mar. Petrol. Geol.* 140, 105674. <https://doi.org/10.1016/j.marpetgeo.2022.105674>.
- Qi, Y., Cai, C.F., Sun, P., Wang, D.W., Zhu, H.J., 2023. Crude oil cracking in deep reservoirs: a review of the controlling factors and estimation methods. *Pet. Sci.* 20, 1978–1997. <https://doi.org/10.1016/j.petsci.2023.03.006>.
- Qiu, N.S., Chang, J., Zuo, Y.H., Wang, J.Y., Li, H.L., 2012. Thermal evolution and maturation of lower Paleozoic source rocks in the Tarim Basin, northwest China. *AAPG (Am. Assoc. Pet. Geol.) Bull.* 96, 789–821. <https://doi.org/10.1306/0907111029>.
- Reiser, J., McGregor, E., Jones, J., Enick, R., Holder, G., 1996. Adamantane and diamantane; phase diagrams, solubilities, and rates of dissolution. *Fluid Phase Equilib.* 117, 160–167. [https://doi.org/10.1016/0378-3812\(95\)02949-4](https://doi.org/10.1016/0378-3812(95)02949-4).
- Scarlett, A.G., Spaak, G., Mohamed, S., Plet, C., Grice, K., 2019. Comparison of tri-, tetra- and pentacyclic caged hydrocarbons in Australian crude oils and condensates. *Org. Geochem.* 127, 115–123. <https://doi.org/10.1016/j.orggeochem.2018.11.010>.
- Schulz, L.K., Wilhelm, A., Rein, E., Steen, A.S., 2001. Application of diamondoids to distinguish source rock facies. *Org. Geochem.* 32, 365–375. [https://doi.org/10.1016/S0146-6380\(01\)00003-1](https://doi.org/10.1016/S0146-6380(01)00003-1).
- Song, Z.Z., Zhang, J., Jin, S.G., Liu, C.Q., Abula, A., Hou, J.K., Ma, L., 2024. The occurrences and mobility of shale oil in the pore space of terrestrial shale. *Fuel* 374, 132377. <https://doi.org/10.1016/j.fuel.2024.132377>.
- Spaak, G., Edwards, D.S., Grosjean, E., Scarlett, A.G., Rollet, N., Grice, K., 2020. Identifying multiple sources of petroleum fluids in Browse Basin accumulations using diamondoids and semi-volatile aromatic compounds. *Mar. Petrol. Geol.* 113, 104091. <https://doi.org/10.1016/j.marpetgeo.2019.104091>.
- Spanu, L., Donadio, D., Hohl, D., Schwegler, E., Galli, G., 2011. Stability of hydrocarbons at deep Earth pressures and temperatures. In: *Proceedings of the National Academy of Sciences*, vol. 108, pp. 6843–6846. <https://doi.org/10.1073/pnas.1014804108>.

- Tian, H., Wang, Z.M., Xiao, Z.Y., Li, X.Q., Xiao, X.M., 2006. Oil cracking to gases: kinetic modeling and geological significance. *Chin. Sci. Bull.* 51, 2763–2770. <https://doi.org/10.1007/s11434-006-2188-8>.
- Tissot, B.P., Welte, D.H., SpringerLink, 1984. *Petroleum Formation and Occurrence*. 2nd, Rev. And Enl. Springer-Verlag, New York;Berlin.
- van der Ploeg, R., Pureveen, J.B.M., van den Boorn, S.H.J.M., van Bergen, P.F., 2023. Novel diamondoid-based maturity models using naturally occurring petroleum fluids. *AAPG (Am. Assoc. Pet. Geol.) Bull.* 107, 1799–1810. <https://doi.org/10.1306/06272323003>.
- Vinnichenko, G., Hope, J.M., Jarrett, A.J.M., Williams, N., Brocks, J.J., 2021. Reassessment of thermal preservation of organic matter in the Paleoproterozoic McArthur River (HYC) Zn-Pb ore deposit, Australia. *Ore Geol. Rev.* 133, 104129. <https://doi.org/10.1016/j.oregeorev.2021.104129>.
- Walters, C.C., Sun, X., Zhang, T.W., 2023. Geochemistry of oils and condensates from the lower Eagle Ford formation, south Texas. Part 4: diamondoids. *Mar. Petrol. Geol.* 154, 106308. <https://doi.org/10.1016/j.marpetgeo.2023.106308>.
- Wang, D., Cai, C., Yun, L., Liu, J., Sun, P., Jiang, Z., Peng, Y., Zhang, H., Wei, T., Pei, B., 2023a. Controls on petroleum stability in deep and hot reservoirs: a case study from the Tarim Basin. *Mar. Petrol. Geol.* 147, 106014. <https://doi.org/10.1016/j.marpetgeo.2022.106014>.
- Wang, Q., Hao, F., Niu, C.M., Zou, H.Y., Miao, Q.Y., Yin, J., Cao, Y.J., Liu, M.X., 2021. Origins and deep petroleum dynamic accumulation in the southwest part of the Bozhong depression, Bohai Bay Basin: insights from geochemical and geological evidences. *Mar. Petrol. Geol.* 134, 105347. <https://doi.org/10.1016/j.marpetgeo.2021.105347>.
- Wang, S., Liu, H., Deng, X.L., Zhu, Y.F., Zhang, Y.T., Zhao, S., Su, Y.H., 2023b. Genetic mechanism of multiphase states of Ordovician oil and gas reservoirs in Fuman oilfield, Tarim Basin, China. *Mar. Petrol. Geol.* 157, 106449. <https://doi.org/10.1016/j.marpetgeo.2023.106449>.
- Wang, W., Li, Y., Xiong, Y.Q., Jiang, W.M., 2023c. Thermal stability of diamondoids and their geological significance. *Geochimica* 52, 29–40. <https://doi.org/10.19700/j.0379-1726.2023.01.003> (in Chinese).
- Wang, Y.P., Zhang, S.C., Wang, F.Y., Wang, Z.Y., Zhao, C.Y., Wang, H.J., Liu, J.Z., Lu, J.L., Geng, A.S., Liu, D.H., 2006. Thermal cracking history by laboratory kinetic simulation of Paleozoic oil in eastern Tarim Basin, NW China, implications for the occurrence of residual oil reservoirs. *Org. Geochem.* 37, 1803–1815. <https://doi.org/10.1016/j.orggeochem.2006.07.010>.
- Wei, Z.B., Moldowan, J.M., Dahl, J., Goldstein, T.P., Jarvie, D.M., 2006a. The catalytic effects of minerals on the formation of diamondoids from kerogen macromolecules. *Org. Geochem.* 37, 1421–1436. <https://doi.org/10.1016/j.orggeochem.2006.07.006>.
- Wei, Z.B., Moldowan, J.M., Jarvie, D.M., Hill, R., 2006b. The fate of diamondoids in coals and sedimentary rocks. *Geology* 34, 1013–1016. <https://doi.org/10.1130/G22840A.1>.
- Wei, Z.B., Moldowan, J.M., Paytan, A., 2006c. Diamondoids and molecular biomarkers generated from modern sediments in the absence and presence of minerals during hydrous pyrolysis. *Org. Geochem.* 37, 891–911. <https://doi.org/10.1016/j.orggeochem.2006.04.008>.
- Wei, Z.B., Moldowan, J.M., Fago, F., Dahl, J., Cai, C., Peters, K., 2007a. Origins of thiadiamondoids and diamondoidthiols in petroleum. *Energy & Fuels* 21 (6), 3431–3436. <https://doi.org/10.1021/ef7003333>.
- Wei, Z.B., Moldowan, J.M., Peters, K.E., Wang, Y., Xiang, W., 2007b. The abundance and distribution of diamondoids in biodegraded oils from the San Joaquin Valley: implications for biodegradation of diamondoids in petroleum reservoirs. *Org. Geochem.* 38, 1910–1926. <https://doi.org/10.1016/j.orggeochem.2007.07.009>.
- Wei, Z.B., Moldowan, J.M., Zhang, S.C., Hill, R., Jarvie, D.M., Wang, H., Song, F., Fago, F., 2007c. Diamondoid hydrocarbons as a molecular proxy for thermal maturity and oil cracking: geochemical models from hydrous pyrolysis. *Org. Geochem.* 38, 227–249. <https://doi.org/10.1016/j.orggeochem.2006.09.011>.
- Xu, H.Y., Liu, Q.Y., Zhu, D.Y., Peng, W.L., Meng, Q.Q., Wang, J.B., Shi, J.Y., Jin, Z.J., 2022. Molecular evidence reveals the presence of hydrothermal effect on ultra-deep-preserved organic compounds. *Chem. Geol.* 608, 121045. <https://doi.org/10.1016/j.chemgeo.2022.121045>.
- Yang, P., Liu, K.Y., Liu, J.L., Yu, S., Yu, B., Hou, M.G., Wu, L.L., 2021. Petroleum charge history of deeply buried carbonate reservoirs in the Shuntuoguole Low Uplift, Tarim Basin, west China. *Mar. Petrol. Geol.* 128, 105063. <https://doi.org/10.1016/j.marpetgeo.2021.105063>.
- Yang, S.F., Chen, H.L., Li, Z.L., Li, Y.Q., Yu, X., Li, D.X., Meng, L.F., 2013. Early permian Tarim large igneous Province in northwest China. *Sci. China Earth Sci.* 56, 2015–2026. <https://doi.org/10.1007/s11430-013-4653-y>.
- Zhan, Z.W., Wang, G.X., Tian, Y.K., Zhan, X., Liang, T., Wang, Y.P., Zou, Y.R., Peng, P.A., 2023. Determination and petroleum geochemical significance of short-chain alkylbenzenes in lacustrine source rocks. *Org. Geochem.* 185, 104685. <https://doi.org/10.1016/j.orggeochem.2023.104685>.
- Zhang, S.C., Huang, H.P., Xiao, Z.Y., Liang, D.G., 2005. Geochemistry of palaeozoic marine petroleum from the Tarim Basin, NW China. Part 2: maturity assessment. *Org. Geochem.* 36, 1215–1225. <https://doi.org/10.1016/j.orggeochem.2005.01.014>.
- Zhang, S.C., Huang, H.P., Su, J., Liu, M., Zhang, H.F., 2014. Geochemistry of alkylbenzenes in the paleozoic oils from the Tarim Basin, NW China. *Org. Geochem.* 77, 126–139. <https://doi.org/10.1016/j.orggeochem.2014.10.003>.
- Zhang, S.C., Hanson, A.D., Moldowan, J.M., Graham, S.A., Liang, D.G., Chang, E., Fago, F., 2000. Paleozoic oil–source rock correlations in the Tarim basin, NW China. *Org. Geochem.* 31, 273–286. [https://doi.org/10.1016/S0146-6380\(00\)00003-6](https://doi.org/10.1016/S0146-6380(00)00003-6).
- Zhang, S.C., Su, J., Wang, X.M., Zhu, G.Y., Yang, H.J., Liu, K.Y., Li, Z.X., 2011. Geochemistry of Palaeozoic marine petroleum from the Tarim Basin, NW China: Part 3. Thermal cracking of liquid hydrocarbons and gas washing as the major mechanisms for deep gas condensate accumulations. *Org. Geochem.* 42, 1394–1410. <https://doi.org/10.1016/j.orggeochem.2011.08.013>.
- Zhang, Z.Y., Zhang, Y.J., Zhu, G.Y., Han, J.F., Chi, L.X., 2019. Variations of diamondoids distributions in petroleum fluids during migration induced phase fractionation: a case study from the Tazhong area, NW China. *J. Petrol. Sci. Eng.* 179, 1012–1022. <https://doi.org/10.1016/j.petrol.2019.05.016>.
- Zhang, Z.Y., Zhu, G.Y., Zhang, Y.J., Han, J.F., Li, T.T., Wang, E.Z., Greenwood, P., 2018. The origin and accumulation of multi-phase reservoirs in the east Tabei uplift, Tarim Basin, China. *Mar. Petrol. Geol.* 98, 533–553. <https://doi.org/10.1016/j.marpetgeo.2018.08.036>.
- Zheng, T.Y., Zhang, Q., Deng, E.D., 2023. Applications of low molecular weight polycyclic aromatic hydrocarbons (PAHs) and diamondoids ratios/indices on the maturity assessment of coal-bearing source rock: insight from mature to overmature Longtan Shale. *Int. J. Coal Geol.* 269, 104209. <https://doi.org/10.1016/j.coal.2023.104209>.
- Zhou, C.X., Yu, S., Huang, W.Y., Zhang, H.Z., Xiao, Z.Y., Zeng, L.F., Huang, W.K., Pan, C.C., 2021. Oil maturities, mixing and charging episodes in the cratonic regions of the Tarim Basin, NW China: insight from biomarker and diamondoid concentrations and oil bulk properties. *Mar. Petrol. Geol.* 126, 104903. <https://doi.org/10.1016/j.marpetgeo.2021.104903>.
- Zhu, G.Y., Li, J.F., Zhang, Z.Y., Wang, M., Xue, N., He, T., Zhao, K., 2020. Stability and cracking threshold depth of crude oil in 8000 m ultra-deep reservoir in the Tarim Basin. *Fuel* 282, 118777. <https://doi.org/10.1016/j.fuel.2020.118777>.
- Zhu, G.Y., Milkov, A.V., Zhang, Z.Y., Sun, C.H., Zhou, X.X., Chen, F.R., Han, J.F., Zhu, Y.F., 2019a. Formation and preservation of a giant petroleum accumulation in superdeep carbonate reservoirs in the southern Halahatang oil field area, Tarim Basin, China. *AAPG (Am. Assoc. Pet. Geol.) Bull.* 103, 1703–1743. <https://doi.org/10.1306/11211817132>.
- Zhu, G.Y., Zhang, Z.Y., Milkov, A.V., Zhou, X.X., Yang, H.J., Han, J.F., 2019b. Diamondoids as tracers of late gas charge in oil reservoirs: example from the Tazhong area, Tarim Basin, China. *Fuel* 253, 998–1017. <https://doi.org/10.1016/j.fuel.2019.05.030>.
- Zhu, G.Y., Zhang, Z.Y., Zhou, X.X., Li, T.T., Han, J.F., Sun, C.H., 2019c. The complexity, secondary geochemical process, genetic mechanism and distribution prediction of deep marine oil and gas in the Tarim Basin, China. *Earth Sci. Rev.* 198, 102930. <https://doi.org/10.1016/j.earscirev.2019.102930>.
- Zhu, X.J., Chen, J.F., Zhang, C., Wang, Y.X., Liu, K.X., Zhang, T., 2021. Effects of evaporative fractionation on diamondoid hydrocarbons in condensates from the xihu sag, east China sea shelf basin. *Mar. Petrol. Geol.* 126, 104929. <https://doi.org/10.1016/j.marpetgeo.2021.104929>.